Doctoral Dissertation

# A Study on Primary Water Stress Corrosion Cracking Behavior of Forged Alloy 600 in Nuclear Power Plant

Seung Chang Yoo

Department of Nuclear Engineering

Graduate School of UNIST

2019

# A Study on Primary Water Stress Corrosion Cracking Behavior of Forged Alloy 600 in Nuclear Power Plant

Seung Chang Yoo

Department of Nuclear Engineering

Graduate School of UNIST

Doctoral Dissertation

# A Study on Primary Water Stress Corrosion Cracking Behavior of Forged Alloy 600 in Nuclear Power Plant

A dissertation
submitted to the Graduate School of UNIST
in partial fulfillment of the
requirements for the degree of
Doctor of Philosophy

Seung Chang Yoo

07. 12. 2019

Approved by

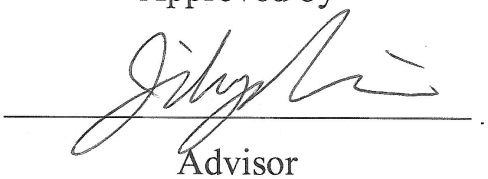

Advisor

Ji Hyun Kim

# A Study on Primary Water Stress Corrosion Cracking Behavior of Forged Alloy 600 in Nuclear Power Plant

Seung Chang Yoo

This certifies that the dissertation of Seung Chang Yoo is approved.

07. 12. 2019

Advisor: Ji Hyun Kim

Il Soon Hwang

Soon Yong Kwon

Young Jin Oh

Min Jae Choi

# ABSTRACT

Primary water stress corrosion cracking (SCC) of nickel-based alloys was frequently reported in several parts in pressurized water reactors (PWRs) and investigated in recent 30 years. However, several factors were missing in most of studies; long-term thermal aging simulation at low, proper temperature and multi-axial stress component induced on the specimen. Also, many proposed models do not fully cover the effect of microstructural changes caused by above two missing factors. Therefore, in this research, method to evaluate the effect of long-term thermal aging and triaxial stress on the PWSCC initiation of nickel-based alloy Alloy 600 was developed. And several parameters were carried out which could be inserted to proposed PWSCC initiation models and make it consider the effect of long-term thermal aging and triaxial stress.

Forging grade Alloy 600 provided by Doosan Heavy Industries & Construction Co., Ltd was used for this study. It was thermally aged at 400 ℃ which is one of the highest temperatures that would not cause any unexpected changes those will not be caused during actual operation environment of nuclear power plant. 10 years and 20 years of thermally aged specimens were simulated by heat treatment.

Triaxial stress was applied to the specimen by making a round notch on the surface of specimen. Stress analysis was conducted to optimize the depth of notches and 33% area reduction was selected. By that, the surface of notch was calculated to have triaxiality of 0.5, while smooth specimen which have no notch have triaxiality of 0.33.

Microstructure, mechanical properties, corrosion resistance, grain orientation were investigated in detail. Major change caused by long-term thermal aging was strength of materials. The tensile properties of 10 years thermally aged specimen were the highest, while elongation of it was the minimum.

Also, the morphology of precipitates was significantly influence by thermal aging. The length of precipitates was not changed while the number fraction of that was increased during 10 years of thermal aging. Meanwhile, length of precipitates was increased and number fraction of that was not changed during 20 years of thermal aging.

Susceptibility to PWSCC was evaluated via slow strain rate test and U-bend test in simulated PWR environment. From the experiment with smooth specimen, it was revealed that 10 years of thermally aged specimen has the highest susceptibility to PWSCC initiation. However, the trend was different in notched specimen; 20 years of thermally aged specimen has the highest susceptibility to PWSCC initiation.

Change of mechanical properties could be explained by Orowan mechanism which is related to the amount of precipitation hardening. From calculation with the values of precipitate morphology, it was found that 10 years of thermally aged specimen would have the highest yield strength; same result with tensile test. Also, it is well-known that yield strength is closely related to PWSCC initiation of nickel-based alloys. From that fact, the parameter of Orowan mechanism was used as the factor which could make the model consider the precipitate hardening effect caused by long-term thermal aging.

Meanwhile, the cracks were observed not at the center of notch of notched specimen; those were observed at the region away from that. It was revealed from stress analysis that the cracked region has high shear stress component than the notch center. Also, from the cracked surface of notched specimen, stair shape of fracture surface was observed. This feature was known to be formed by highly localized plasticity where shear stress is high, or hydrogen permeate is severe. From this observation, it could be thought that shear stress has severe influence on PWSCC initiation. Therefore, critical resolved shear stress which is the parameter that signified the resistance of material to shear stress was calculated. And calculation result has same trend with that of PWSCC initiation of notched specimen. So, it was used as the factor which could make the model consider the effect of shear stress caused by triaxial stress.

Two parameters were deduced from the study; parameter from Orowan Mechanism and from critical resolved shear stress. Those were inserted to initiation model of Garud and seems fitted well with several previous experimental results. However, the use of the model could be limited by following assumptions and realities: many PWSCC initiation studies do not deep investigation about precipitate morphologies or stress components. Without this information, it is hard to be calculated by proposed model of this study. Also, it is hard to control the morphology of precipitates via heat treatment and PWSCC initiation experiment itself is difficult and time-consuming test.

Nonetheless, this research emphasize that the morphology of precipitates could influence not only strength of material, but also change PWSCC initiation susceptibility under various stress conditions. Also, triaxial stress and corresponding shear stress could change the susceptibility to PWSCC initiation of Alloy 600.

# CONTENTS

# NOMENCLATURE

*Abbreviations*

| | |
|---|---|
| ASTM | American Society for Testing and Materials |
| CRSS | Critical Resolved Shear Stress |
| CSL | Coincidence Site Lattice |
| CSM | Continuous Stiffness Measurement |
| DCPD | Direct Current Potential Drop |
| EBSD | Electron Back Scatter Diffraction |
| EDS | Energy-Dispersive X-ray Spectroscopy |
| FIB | Focused Ion Beam |
| IGSCC | Intergranular Stress Corrosion Cracking |
| KAM | Kernel Average Misorientation |
| PWR | Pressurized Water Reactor |
| PWSCC | Primary Water Stress Corrosion Cracking |
| SCC | Stress Corrosion Cracking |
| SEM | Scanning Electron Microscope |
| SHE | Standard Hydrogen Electrode |
| SSRT | Slow Strain Rate Test |
| TEM | Transmission Electron Microscope |
| TTT | Time-Temperature-Transformation |

*Greek Symbols*

| | |
|---|---|
| $\lambda_e$ | Non-cold work related factor |
| $A$ | Cold work-SCC microcracking resistance |
| $z$ | Cold work-SCC threshold |
| $r$ | Strength ratio |
| $\sigma$ | Applied stress |
| $\sigma_y$ | Yield stress |
| $\sigma_u$ | Ultimate tensile stress |
| $m$ | Measure of cold work |
| $E$ | Young's modulus |
| q | Empirical constant defining $a_n$ in terms of m |
| $a_n$ | Cold work-SCC environmental resistance |
| $a, b, c, k, z_1, z_2$ | Empirical constants |
| T | Temperature |
| r | Radius of Precipitates |
| t | Elapsed Time |
| $t_{aging}$ | Heat Treatment Time at Simulated Thermal Aging Temperature |
| $t_{ref}$ | Service Time at Nuclear Power Plant |
| Q | Activation Energy |
| R | Gas Constant |
| $\boldsymbol{\tau}$ | Cut/bowing Stress of Orowan Mechanism |
| $\boldsymbol{G}$ | Shear Modulus |
| $\boldsymbol{b}$ | Magnitude of Burgers Vector |
| D | Distance Between Precipitates |
| V | Volume Fraction of Precipitates |

| | |
|---|---|
| Z | Distance Between Precipitates in z direction |
| O | Parameter for Orowan mechanism |
| C | Parameter for Critical Resolved Shear Stress |

# LIST OF FIGURES

# LIST OF TABLES

# 1. INTRODUCTION

## 1.1. Background and motivation of Research

Nickel-based alloys are frequently used for the components which are used under challenging operational environments such as high temperature, severe stress owing to weld residual stress or thermal stress, and oxidizing environments, such as gas turbine engines, chemical processing plants and most generally, power plant systems as shown in Figure 1-1. These components were decided to be fabricated with nickel-based alloys since those alloys have higher resistance to most of degradation mechanisms under the conditions. However, several types of failure were reported in those parts such as stress corrosion cracking (SCC), fatigue and low cycle fatigue [1]–[5]. Localized oxidation at grain boundaries was known to be a reason for crack nucleation and propagation of low cycle fatigue [3]. For creep, precipitates coarsening due to exposure to high temperature was reported as important factor losing creep resistance [4]. But understanding about failure mechanisms such as SCC is lacking since it is occurred by complicated combination of several characteristics such as material susceptibility, corrosion environment and tensile stress or residual stress. Many researches were performed to understand SCC, however, many experts still think that there exist many uncertainties regarding SCC [6]–[8]. To find out the missing point in SCC studies, literature survey was conducted as below.

Most of alloys used in nuclear power plant are austenitic nickel-based alloys; Alloy 600, 690, 800, and so on. Those alloys are known to have Ti, Nb, Cr precipitates. Ti and Cr precipitates at grain boundary while Nb precipitates at matrix. Those precipitates are known to have significant effect to material properties. Precipitates generally formed during heat treatment and could be estimated from phase diagram or time-temperature-transformation diagram. Figure 1-2 shows the ternary phase diagram of Ni-Fe-Cr alloy. Alloy 600, 690 and associated weld metals are expected to become a single phase austenitic alloy [9]. From the diagram, it could be thought that no other phase would be present except the Cr carbide precipitation. As temperature increased to solution annealing or thermal treatment temperature (600 ~ 1200 ℃), no secondary phase transformation occurs according to phase diagram. Therefore, carbide precipitation is the only problem which will be caused during heat treatment in terms of phase of material.

Important phenomenon caused by precipitation is chromium depletion near the carbides and grain boundary. As shown in Figure 1-3, carbide formation at grain boundary causes depletion of chromium near it. Chromium depletion in the matrix near grain boundaries could be occurred during thermal treatment depending on carbon contents. The degree of sensitization is dependent on heat treatment temperature and duration. Chromium diffusion is faster at grain boundary than substitutional diffusion in grain matrix resulting in chromium depletion near grain boundaries [10]. In general, thermal treatment to recover chromium depletion is conducted at least 700 ℃ for around 20 hours. Longer time

would be needed to recover it at lower temperature [11].

To reveal the details of Alloy 600 during thermal aging at operation temperature, tremendous studies were conducted with consideration of above factors. Most of studies were focused on microstructure and mechanical properties and tries to connect those with SCC susceptibility of Alloy 600. Kai et al. [12] investigated several changes observed in nickel-based alloys during various heat treatment conditions. Increment of corrosion resistance was observed during heat treatment and chromium carbide was reported as a reason for this increment. Celin et al. [13] also investigate the degradation mechanism of nickel-based alloys and summarized that those nickel-based alloys are expected to have a problem after used for long-term operation. Also, Electric Power Research Institute conducted a study about control rod drive mechanism of Davis-Besse reactor, where SCC was occurred and leaked boron acid causes degradation of pressure vessel [14], [15]. Including these researchers, several studies report that material change during heat treatment by operation temperature significantly influenced to material degradation of nickel-based alloys. The degradation of material due to exposure to high temperature is called thermal aging.

As explained above, thermal aging was emphasized as one of important degradation mechanism occurred during operation and studied by many researchers. And many studies found that material properties were influenced by long-term thermal aging. However, there exist a question about the method they used to determine heat treatment temperature. Most of the studies used the temperature above 600 ℃ [16]–[21]. But these temperature range is not persuasive since the operation temperature of nuclear power plant is around 320 ℃. As proposed by several studies, grain boundary diffusion is dominant at temperature around 320 ℃, while volume or matrix diffusion is dominant at high temperature above 600 ℃ [17], [22]. As shown in Figure 1-4, time-temperature-transformation curve of Alloy 600 is generally drawn at the temperature region above 600 ℃. These mean that it is hard to know what is happened at long-term exposure to low temperature around 320 ℃. However, huge difference is expected in terms of phases and degradation mechanism between thermally aged material at low temperature and high temperatures [23]–[32]. Many studies were carried out to investigate the long-term thermal aging effects on dissimilar metal welds with nickel-based alloys, and observed significant effects on material properties during long-term thermal aging at low temperatures (~450 ℃) [9], [31], [33]–[35].

Meanwhile, several testing methods are proposed to evaluate the SCC resistance of structural materials. the most widely used SCC tests are U-bend test and slow strain rate test (SSRT). Both tests were usually conducted in primary water SCC (PWSCC) field, and both are very time consuming and difficult to perform. Nevertheless, SSRT and U-bend test have been successfully used in several environments, including nuclear field.

SSRT technique is a uniaxial tensile test under extremely low displacement rate with corrosive environment. These tests are performed to produce and evaluate either SCC or mechanical failure in corrosive environment. Slow strain rate ensures the crack tip to have enough time for interaction under environment and encourages the initiation or growth of SCC. SCC susceptibility often presented in terms of time to fracture or morphology features of the fracture surface.

SSRT have several important deciding things such as strain rate, surface finishing, testing temperature, pressure, water chemistry, and so on, to properly evaluate PWSCC susceptibility. Especially, strain should be carefully decided to give enough testing speed, repeatability and reproducibility. American society of testing and materials (ASTM) standard suggest using the strain rate of $1 \times 10^{-6}$ or below. This strain rate known to give satisfactory results for nickel and austenitic alloys. The main criticism of the SSRT technique is that specimens undergoes failure at excessive load, making the testing condition too aggressive. Most of tests elongates the specimen up to failure, and necessarily apply too high stress to specimen.

U-bend specimens are a bended specimen fixed with some fixtures to maintain residual stress on the surface of specimen. Because of the simple fabrication procedure, many specimens were usually fabricated and used for the specimen, therefore generate many susceptibility data for alloys which could be used in statistical usage. U-bend test is standardized by ASTM G30, "Standard Practice for Making and Using U-Bend Stress Corrosion Test Specimens.". Using U-bend specimens offers advantage in terms of ease of fabrication and cost, however this represents only a single test condition, with strain at the apex of approximately 13 to 14 percent [36].

As shown in the above, many studies try to evaluate the SCC resistance of several materials with tensile test at high temperature water or U-bend test. However, the stress state at tested region or surface of specimen should be considered. Both U-bend and flat or smooth bar type specimen undergoes its deformation under monoaxial stress state. But as shown in Figure 1-5, and several previous studies [37]–[39], stress induced at cracked area is not simple monoaxial state. Complex stress is induced in those parts due to weld residual stress applied during welding procedure and complex geometry of them. It needs three different coordinates to properly present the stress condition at those components. Therefore, the stress induced could be classified as triaxial stress state.

Triaxial stress state often considered as one of the important parameters in mechanical engineering, when evaluating the fracture strain or toughness of material. Compact tension specimen often used when they measure the J-R behavior of material and compact tension specimen is one of the designs of specimen which undergoes its deformation under triaxial stress state. As shown in Figure 1-6, fracture strain of the material is severely changed with or without triaxial stress applied. It could be thought that SCC behavior also influenced by the fact whether triaxial stress is applied or not. However, as shown

in above studies, it is not considered properly; most of studies just use monoaxial stress to evaluate the SCC resistance of their materials.

SCC mechanism proposed by P. Scott [23] is most widely accepted in this field. Scott et al. do several experiments with nickel-based alloys under various environmental conditions to find relationship of intergranular SCC (IGSCC) with oxidation phenomena. And internal oxidation mechanism was suggested: oxygen diffused along grain boundaries in redox potential environmental and causing SCC. Several attempts were done to evaluate and understand the nature of SCC and susceptibility of nickel-based alloys to SCC initiation and growth based on this mechanism [40], [41]. However, those are expected to be improved if proper consideration about long-term thermal aging and triaxial stress was done. Different diffusion behavior at low temperature and high temperature could change several microstructures of nickel-based alloy, which in terns effect the oxidation behavior and precipitates at grain boundary. Also, triaxial stress induced at surface of material could change the diffusion speed or penetration depth of oxygen through grain boundary.

Based on above mechanism and experiments, SCC initiation model was developed and used. Most well-known one is the model proposed by Garud [42], which have its focus on cold work or mechanical characteristics of material. As shown in the equation below, material characteristics in terms of microstructure which most significantly affected by long-term thermal aging are considered as one single parameter $\lambda_e$. Thi s might be not enough to consider the complex changing of microstructural during long-term thermal aging. Also, this model does not consider the existence of triaxial stress.

$$t_i = \lambda_e \ln[A] \frac{\ln[\frac{A-z}{\sigma/\sigma_y - z}]}{\ln[\frac{A-z}{1-z}] m^q} \quad (1)$$

$\lambda_e$ = Non-cold work related factor

$A$ = Cold work-SCC microcracking resistance $= vexp[wr]$

$z$ = Cold work-SCC threshold $= z_1 + z_2 \ln(r)$

$r$ = Strength ratio $= \frac{\sigma_u}{\sigma_y}$

$\sigma$ = Applied stress

$\sigma_y$ = Yield stress

$\sigma_u$ = Ultimate tensile stress

$m$ = Measure of cold work $= k\left(\frac{S_y}{E}\right)^a (r-1)^b (r)^c$

$E$ = Young's modulus

q = Empirical constant defining $a_n$ in terms of m

$a_n$ = Cold work-SCC environmental resistance $= 1/m^q$

$a, b, c, k, z_1, z_2$ = Empirical constants

## 1.2. Objective

Two big missing points are deduced from literature study; long-term thermal aging at low temperature and triaxial stress applied on the specimen. Both clearly have large influence on SCC resistance of materials, but somewhat overlooked for now in experiments, mechanisms and even in models. It is therefore essential to investigate the effects of those to SCC susceptibility of nickel-based alloy to understand the nature of SCC. For this, long-term thermal aging at low temperature and triaxial stress applied on the surface of specimen were simulated via proper method. And the effect of those was evaluated via experiment. Based on the experimental results, relevant equations were deduced and inserted to Garud model.

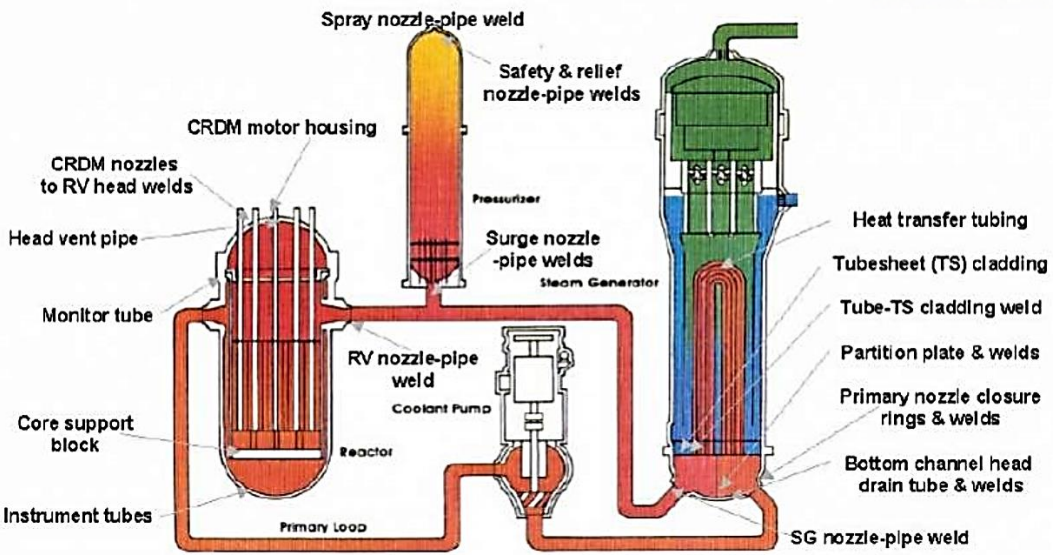


Figure 1-1. Components fabricated with Alloy 600/182/82 in primary circuit of PWR [23]

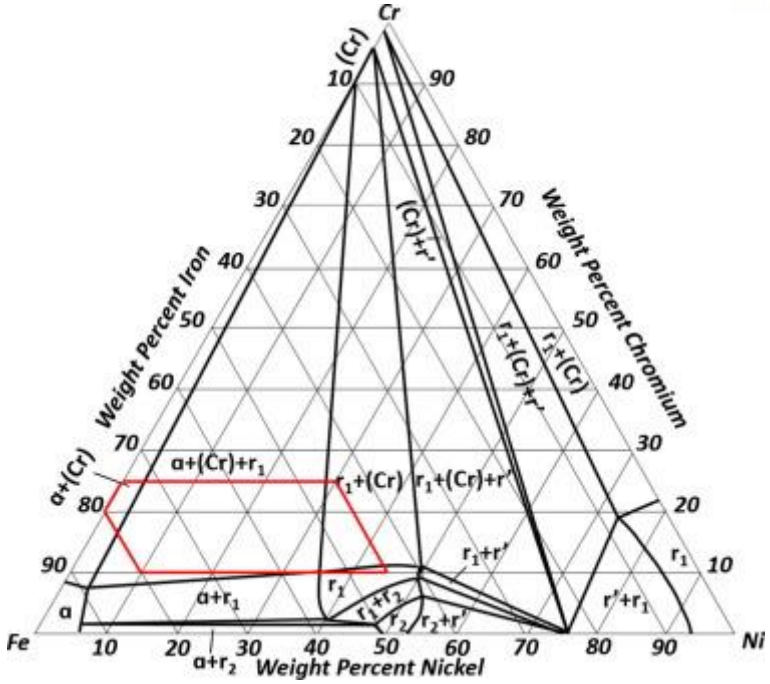


Figure 1-2. Computed isothermal section (377 ℃) of the Cr–Fe–Ni phase diagram [9].

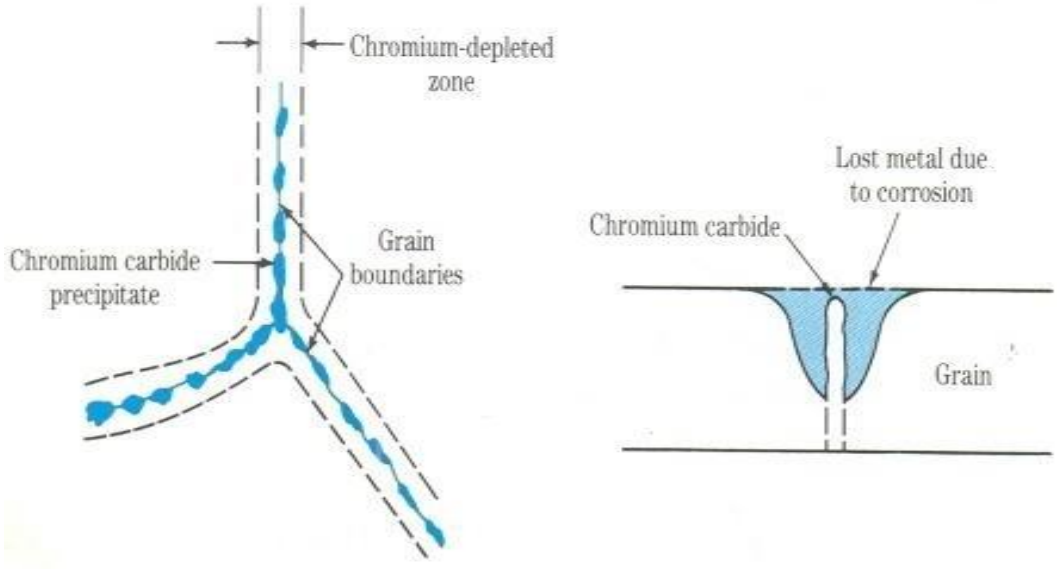


Figure 1-3. (a) Chromium carbide precipitation of grain boundaries (b) Cross section of grain boundary showing intergranular corrosion attack [43]

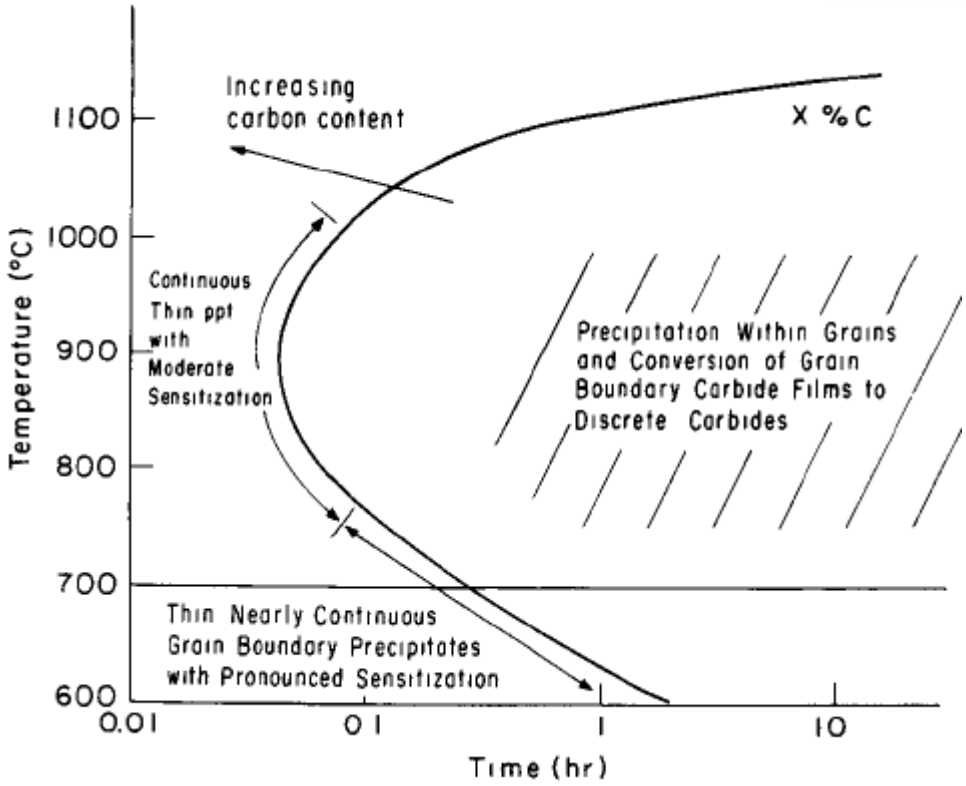


Figure 1-4. Time-temperature-transformation diagram of Alloy 600 [23]

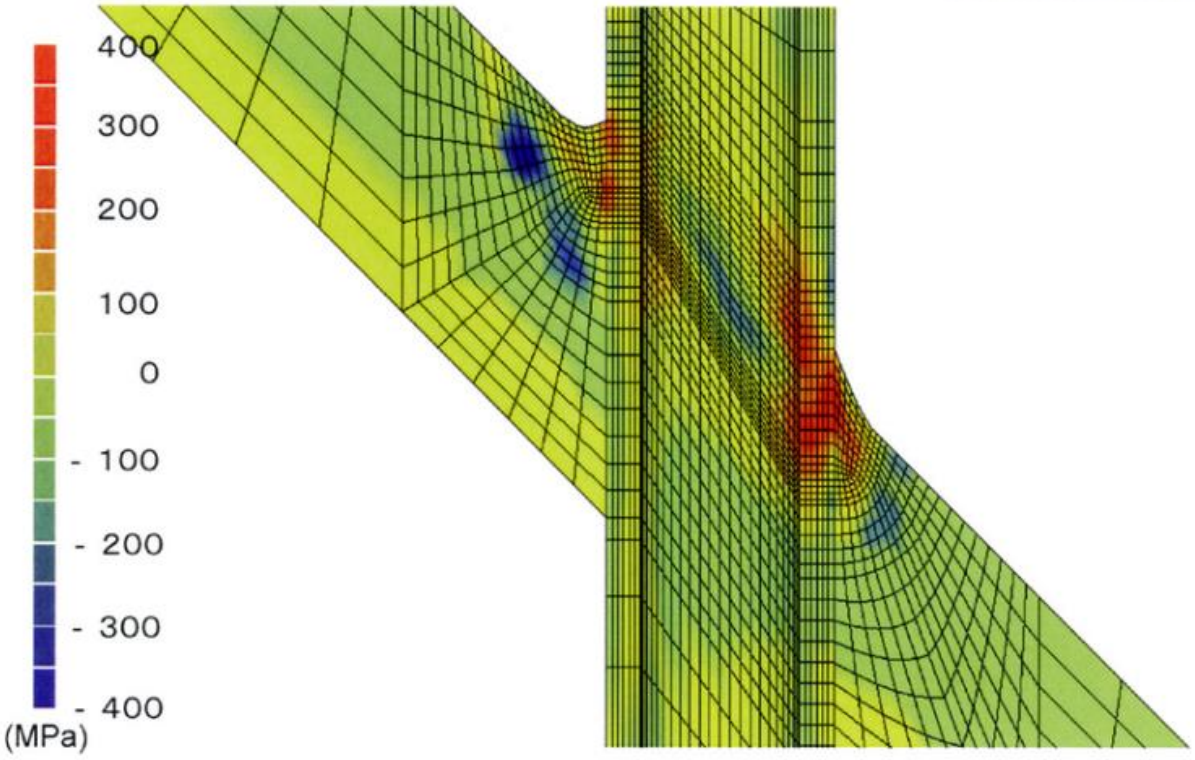


Figure 1-5. Stress analysis at the weld of head penetration nozzle [39]

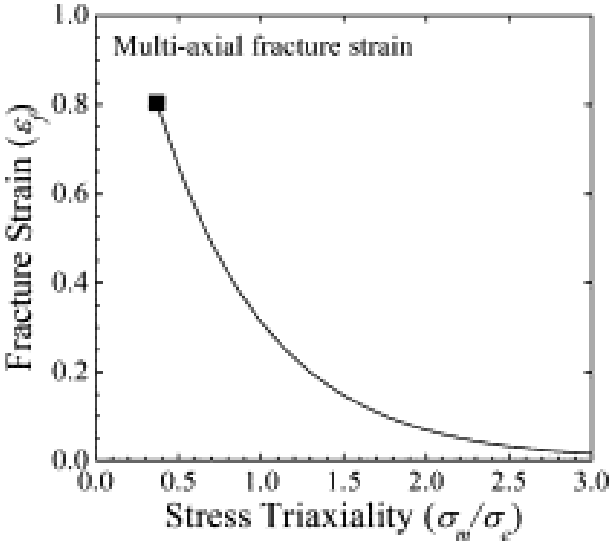


Figure 1-6. Multi-axial fracture strain of nickel-based alloy by stress triaxiality [37]

# 2. Experimental Conditions

## 2.1. Used material and process of thermal aging simulation

Forging grade Alloy 600 was provided by Doosan Heavy Industries & Construction Co. Ltd and used in this study. Thick-walled cylindrical nickel-based Alloy 600 was used in this study, which was fabricated according to ASTM B166 standards. Cylinder was mill annealed at 1060 ℃ for 3.5 h and water quenched. Table 2-1 represents the chemical composition of Alloy 600.

To decide the temperature for long-term thermal aging process, time-temperature-transformation (TTT) diagram was investigated [22]. TTT diagram is shown in Figure 2-1. Several boundary temperatures are marked on the table. During operation, only grain boundary diffusion would be occurred. So, the temperature should be beneath 585 ℃. Also, according to diagram, sensitization could be occurred during long-term heat treatment at above 450 ℃. From these considerations, accelerated temperature was decided to 400 ℃. To assure the phases formed during thermal aging and operation same, stable phases were calculated according to thermodynamics. As shown in Figure 2-2 and Figure 2-3, same phases are stable and will be formed at Alloy 600 containing 0.7 wt. % carbon.

Chromium carbide is always treated as one of the important element in nickel-based alloys which influenced to almost every properties of microstructure and associated mechanical properties [44]. The formation of carbide could be controlled via diffusion speed of chromium, since the diffusion speed of carbon is much faster than that of chromium. Therefore, author decided to simulate the diffusion length of chromium along grain boundary during actual operation in PWR by heat treatment at 400 ℃. For that, duration of thermal aging treatment was decided based on Arrhenius diffusion equation as shown in equation (2). For the activation energy, chromium diffusion activation energy along grain boundary proposed by previous researcher was used [45].

$$\frac{t_{aging}}{t_{ref}} = \exp\left[-\frac{Q\left(\frac{1}{T_{ref}}-\frac{1}{T_{aging}}\right)}{R}\right] \qquad (2)$$

In this equation, $t_{aging}$ is the heat treatment time at 400 ℃, $t_{ref}$ is the service time during operation of PWR and $R$ is the gas constant. The heat treatment temperature 400 ℃ is represented by $T_{aging}$ and $T_{ref}$ is the actual operation temperature of the NPP; 320 ℃. The heat treatment time required at 400 ℃ were then calculated according to equation. Figure 2-4 shows the calculation results according to above equation. From the figure, 1,142 h of heat treatment at 400 ℃ is required to simulate 10 years of

operation thermal aging, and 2,284 h for 20 years of thermal aging.

Then, heat treatment was conducted in Ar environment to simulate the effect of long-term thermal aging in PWR. Three different duration of heat treatment was simulated; 0 years for as received state, 10 and 20 years of thermal aging. Heat treatment at 400 ℃ were conducted for 1,142 and 2,284 h to simulate 10 and 20 equivalent years, respectively. Table 2-2 shows the specimen naming, simulated aging time, and temperature of each specimen; HT400_Y10 for 10 years of thermally aged specimen and HT400_Y20 for 20 years of thermally aged specimen.

## 2.2. Specimen design and triaxial stress

There exists various way to apply triaxial stress on the surface of specimen. Most conventional method is constant stress test with U-bend or C-ring type specimens. There are many benefits for constant load test; if fixture is simple, many specimens could be tested at once, relatively handy for experiment compare to other experiments with active loading system, can be conducted with relatively simple test equipment. However, in long-term test, there exist an issue of stress relaxation due to thermal expansion coefficient difference between specimen and fixture. Also, this kind of constant stress tests required very long time to crack initiation.

SSRT is a powerful replacement of constant load test since it effectively decreases the test duration. SSRT is one of the constant elongation tests that maintain its strain rate constant. For that, round bar type specimen was frequently used by previous studies and authors decide to use round bar type specimen so that easily compare the results of this research with that of previous ones.

To induce triaxial stress on the surface of specimen, as shown in Figure 2-5, round notches were inserted on the surface of specimen. 33%, 50% or more percentage of area reduction rate was first considered as candidate and stress analysis was conducted. From stress analysis, it was found that the triaxial stress applied on the surface was not much changed after area reduction of 33% as shown in Figure 2-6. Too deep notch could cause formation of crevice at the tip of specimen. Therefore, 33% area reduction was selected as the depth of notch to induce triaxial stress on the surface.

From above consideration, smooth bar type specimen under monoaxial stress and notched bar specimen under triaxial stress was fabricated as the blueprint shown in Figure 2-7.

## 2.3. Experimental procedure

### 2.3.1. Mechanical property

Tensile test was performed with INSTRON 8801 universal material testing machine to measure

mechanical properties. Strain rate was determined according to ASTM; 0.4 $min^{-1}$. Extensometer was used to measure the deformation of gage section area only. Specimen used during tensile test was designed via proportional reduction based on the standard design of ASTM E8-E8m since the material amount is limited. 6 tests were conducted for each of thermally aged specimen to reduce experimental error. Fracture surface of every specimen were then analyzed with SEM after tensile test to investigate the failure mode of the materials.

Tensile test could measure bulk properties; however, microstructural changes are important since the changes induced by thermal aging should be micron scale. In order to investigate the mechanical properties in micro- or nanoscale, nanoindentation tests were conducted with Agilent Technologies Nano Indenter G200. To measure the hardness as a function of penetration depth, continuous stiffness measurement (CSM) technique with the Nano Indenter XP head was used. Three-sided pyramidal Berkovich tip was used for every test. Tip geometry is shown in Figure 2-8. To normalize the tip before experiment, calibration procedure was conducted with a fused silica reference material. Total penetration depth of each test was 2000 nm. Strain rate was 0.05 $s^{-1}$. And for Poisson's ratio, 0.3 was used which is a commonly used value during testing of stainless steels or nickel-based alloys. Two 4 x 4 arrays, total 32 points were tested in single specimen at different regions. The size of indentation mark was about 3 ~ 4 microns. The indentations were conducted with the distance of 40 μm to avoid effect of plastic deformation applied during indentation. Total indentation array size was 200 μm x 200 μm for each specimen. Indentation hardness was measured by averaging the values of depths from 1500 nm to 1800 nm of each specimen where relatively flat gradient was observed in results according to previous studies [46]. Then averaged indentation hardness value was deduced in order to achieve precise results.

### 2.3.2. Microstructure

Small samples were fabricated to observe the microstructure and oxide layer of it; dimensions of 10 × 10 × 3 $mm^3$ and cut using electrical discharge machining. The surface finishing was performed. First, surface was grounded with various size of SiC papers up to 800 grit. Then polishing was conducted with diamond pastes from the particle size of 6 μm to 1 μm, then with 0.05 μm colloidal alumina to achieve flatter surface. Then final polishing was conducted with vibratory polisher to remove any residual stress induced during surface finishing.

Microstructural analysis was conducted with specimen prepared by above procedures and then etched to reveal microstructure with 20% HCl in $HNO_3$ etching solution, according to ASTM E407-07 standards Then electron microscopy was observed with scanning electron microscope (SEM) attached Quanta 3D Dual-Beam Focused Ion Beam (FIB). Detail microstructure such as precipitate was

investigated with transmission electron microscope of JEOL, JEM-2100F, with specimen fabricated by FIB. Energy-dispersive X-ray spectroscopy (EDS) attached to SEM and TEM was used to investigate the chemical composition.

The crystal and grain boundary orientations were analyzed via electron backscatter diffraction (EBSD). It was conducted using the same instrument with FIB at 10 kV of acceleration voltage, 4 nA of current, 70° of tilt angle and 17 mm of working distance. Since the size of grain was about 20 μm, step size was selected as 0.5 μm which can measure several points in one grain. Orientation image microscopy software of TSL was used for EBSD result analysis. Scanned area was set as maximum value at the magnification x1000, 597 × 1764 μm, so that cover several numbers of grains to get statistically accurate result of grain and grain boundary misorientation.

### 2.3.3. Corrosion resistance

Immersion corrosion test was conducted to analyze susceptibility to intergranular attack according to ASTM A262 practice C. Specimen was prepared via electrical discharge machining with dimension of 30 x 30 x 3 $mm^3$. Specimens were mechanically grounded with SiC papers up to 800 grit, and diamond paste up to 0.05 μm colloidal silica. Exposed area was controlled to 18 $cm^2$. And it was immersed in 65 wt. % of nitric acids which were controlled to 80 ℃ via water bath with stirrer, then weight loss was measured every 48 h. Morphology of cross section and weight loss rate was then measured at every specimen to analyzed the corrosion characteristics of it.

Corrosion behavior was investigated via electrodynamic method. Potentiodynamic electropolarization was measured with potentiostat of Princeton Applied Research 273A. Three-electrodes were used in electrodynamic cell; platinized platinum mesh was used as counter electrode, saturate calomel electrode was used as reference electrode which have 0.241 V vs. standard hydrogen electrode (SHE) and samples were used as working electrode. Measured area was controlled to 0.785 $cm^2$. Potential sweep was performed at the range from -0.6 V to 1.5 V versus open circuit potential. Open circuit potential was measured in static state where potential fluctuation below 10 mV and sweep rate was 0.1 mV/sec. The electrolyte was prepared with the simulated primary water condition by maintaining the chemicals; boron cations of 1200 mg/kg, lithium cations of 2 mg/kg of lithium cations and purged with high-purity Argon gas to control the concentration of dissolved oxygen in electrolyte.

The oxidation behavior of each thermally aged specimens was investigated with SEM and TEM. Specimens were prepared via the procedures suggested in microstructure analysis. Then, those specimens were exposed to simulated primary water condition which have 1200 mg/kg of boron cations and 2 mg/kg of lithium cations. And the gas concentration was controlled for 25 $cm^3$/kg (dissolved

hydrogen) and below 5 μg/kg (dissolved oxygen), respectively

### 2.3.4. PWSCC susceptibility

Tensile specimens with smooth and notched type was prepared, respectively as shown in Figure 2-9. SSRT was conducted at simulated primary water condition. Water chemistry was controlled by adding $H_3BO_3$ and LiOH which could maintain the concentration of 1200 mg/kg of boron cations and 2 mg/kg of lithium cations. Test temperature were 315 and 340 ℃. The dissolved oxygen concentration was maintained to below 5 ppb. And dissolved hydrogen concentrations were maintained to at 25 $cm^3$/kg. The strain rate was $1.00 \times 10^{-7}$ /sec, according to ASTM G129 standards. The strain rate of smooth and notched specimen was maintained to be same by controlling the displacement rate which calculated via finite element method with the equipment shown in Figure 2-10. Water chemistry was monitored as shown in Figure 2-11, also load and displacement was monitored as shown in Figure 2-12.

6 specimens were tested per one test. Specimens were connected in series at actuator in autoclave system. Every specimen was assumed to be elongated simultaneously before SCC initiation of certain specimen. After SCC initiated in a specimen, it was replaced with dummy specimen which have thicker radius than other specimens so that does not deform during the rest of test. After the test, specimen surface was observed with OM and SEM. Cross sectional analysis was also conducted to observe details near crack tips with FIB attached SEM.

Direct current potential drop (DCPD) method was used to monitor the SCC initiation of each specimen on-line as shown in Figure 2-13. Potential drop was measured with attached two Pt wires and SCC initiation time of each specimen was calculated through the method used in previous studies [47], [48]. Cross sectional area of specimen is reduced due to formation of SCC causing significant change in gradient in DCPD curve. Then the initiation time was calculated; SCC initiation time was decided to inflection point which could be calculated through polynomial fitting. And the surface of the SCC-initiated specimen was analyzed using SEM. Figure 2-14 shows the PWSCC initiated specimen by the method explained above.

Since the tested number of SSRT is relatively small, U-bend test was also conducted. Specimen was prepared as blueprint shown in Figure 2-15. Specimens were immersed to autoclave which was also maintained to primary water condition by same method with SSRT. Specimens were fixed by the cage shown in Figure 2-16. Specimens were designed to have constant stress at the apex region: according to finite element analysis, it was found that stress at apex region was almost maintained if the leg distance is closer enough, exceeding certain critical length. In this design, critical length was 21 mm. Each 6 thermally aged specimens were immersed for 750 h, and surfaces were observed with

optical microscope.

Table 2-1. Chemical composition of Alloy 600 used in this study [34].

| Element | C | Si | Mn | Cr | Cu | Ni | S | Fe |
|---|---|---|---|---|---|---|---|---|
| wt.% | 0.07 | 0.33 | 0.56 | 15.83 | 0.02 | 74.79 | <0.001 | 8.40 |

Table 2-2. Specimen name, aging time and temperature of each aged specimen [34].

| Specimen name | Simulated aging time and temperature | Heat treatment time and temperature |
|---|---|---|
| As received | - | - |
| HT400_Y10 | 10 years at 320°C | 1142 hours at 400°C |
| HT400_Y20 | 20 years at 320°C | 2284 hours at 400°C |

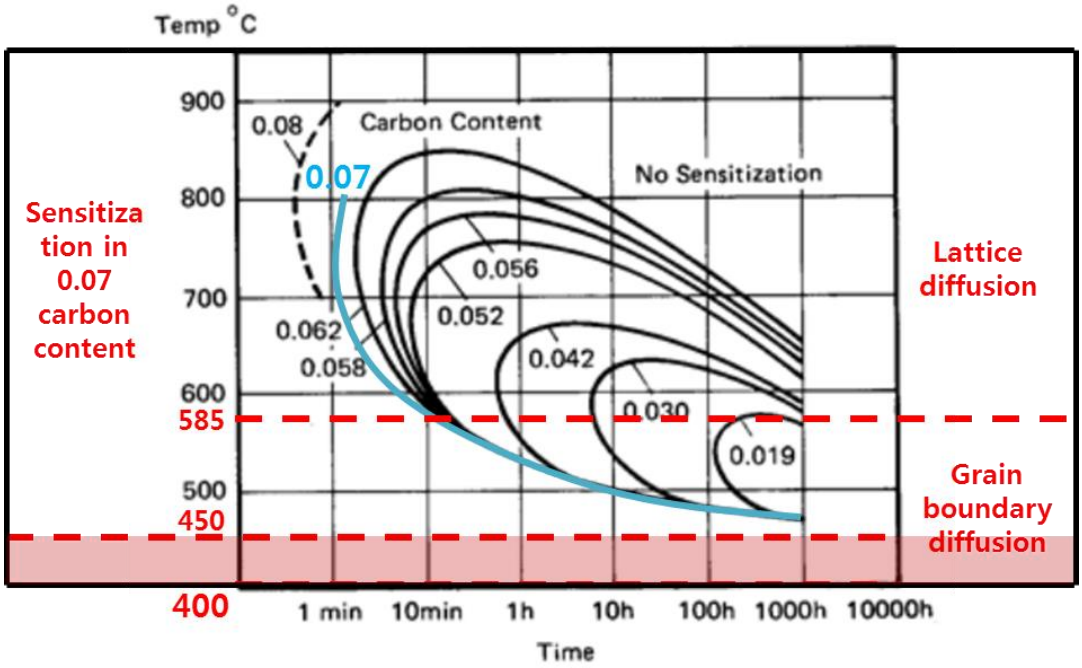


Figure 2-1. Time-Temperature-Transformation diagram of Alloy 600 with different carbon contents [22]. Several criteria were marked in the diagram. 585 ℃ is boundary temperature of lattice and grain boundary diffusion. And above 450 ℃, sensitization could be occurred during long-term thermal aging.

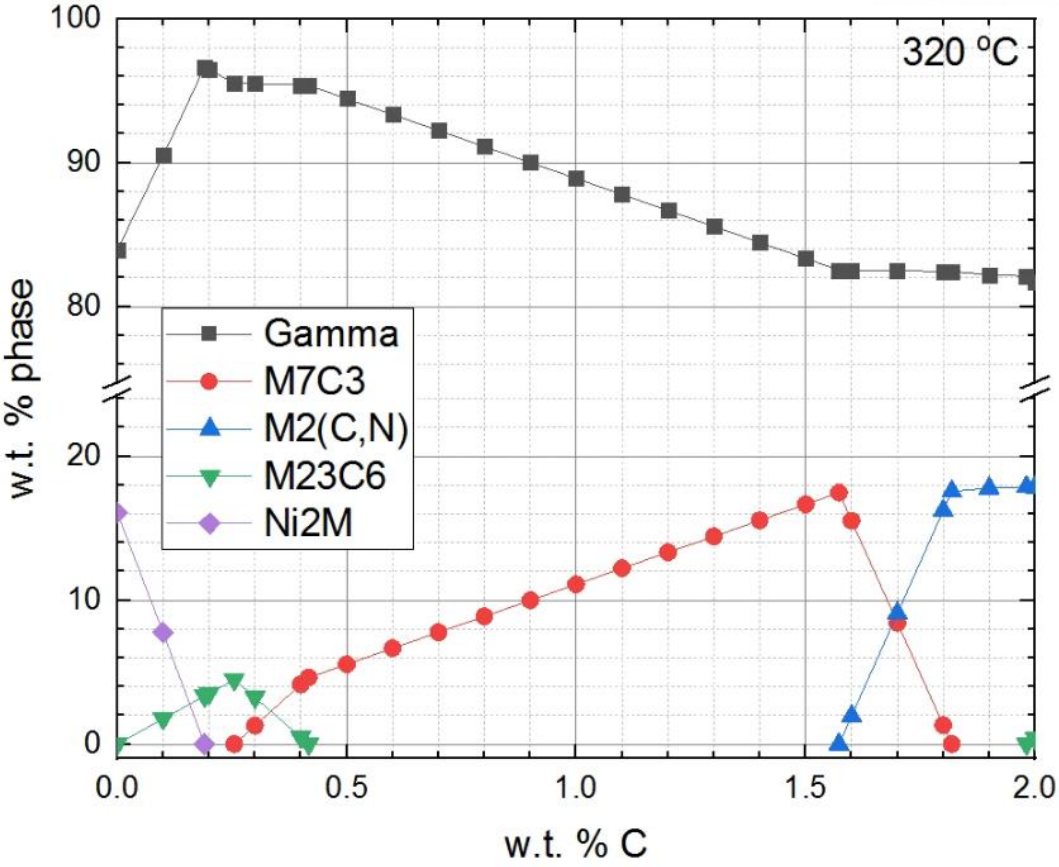


Figure 2-2. Thermodynamic phase diagram of Alloy 600 used in this study at 320 ℃.

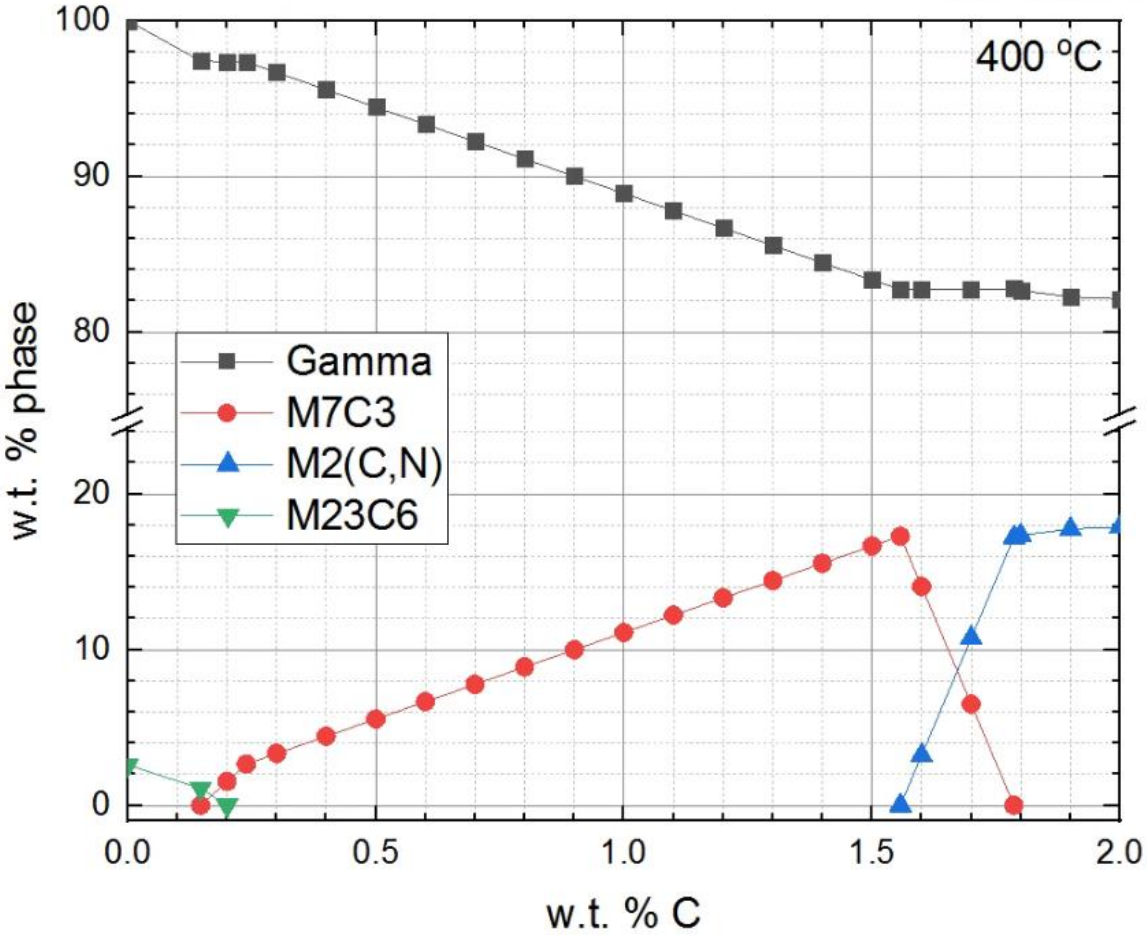


Figure 2-3. Thermodynamic phase diagram of Alloy 600 used in this study at 400 ℃.

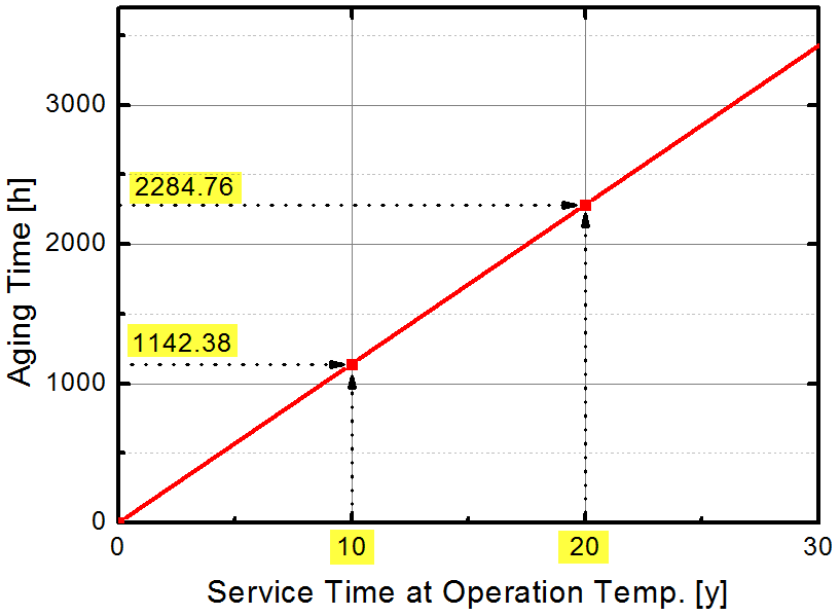


Figure 2-4. Required thermal aging time at 400 ℃ to simulate service time at operation temperature (320 ℃) [34].

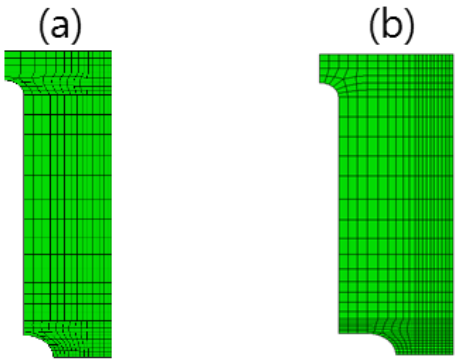


Figure 2-5. Finite element model to calculate triaxiality imposed on the surface and center elements. (a) 33% area reduction model, (b) 50% area reduction model.

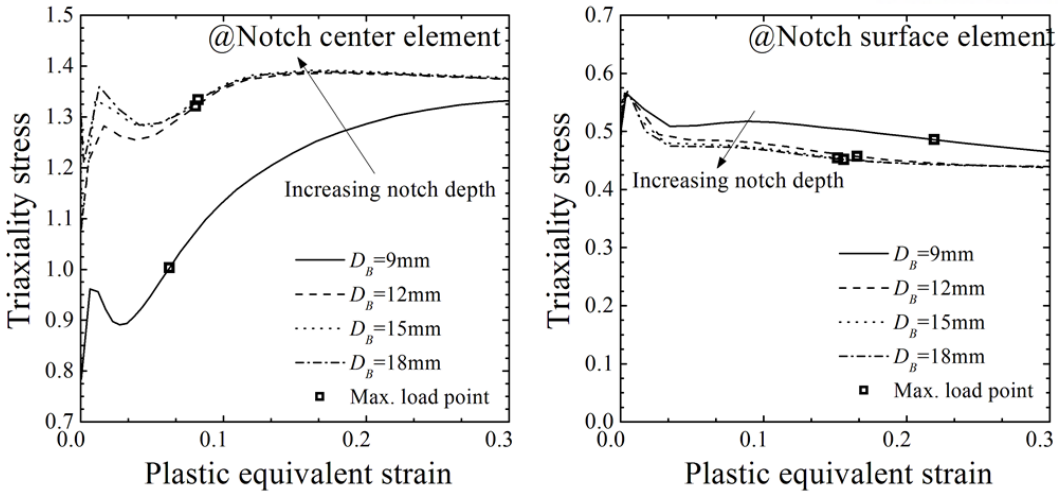


Figure 2-6. Stress analysis results of notch center element and surface element of the models shown in Figure 2-5.

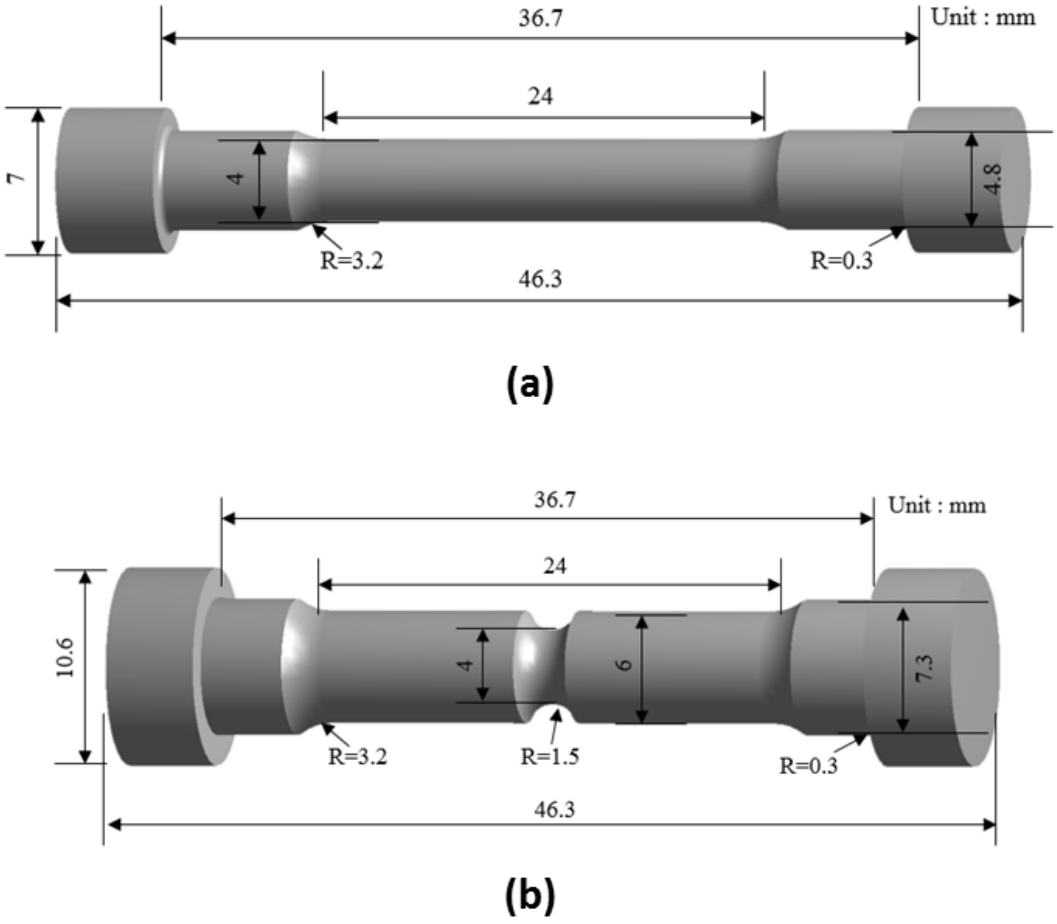


Figure 2-7. Specimen design for monoaxial and triaxial stress state; (a) smooth specimen under monoaxial stress and (b) notched specimen under triaxial stress [35].

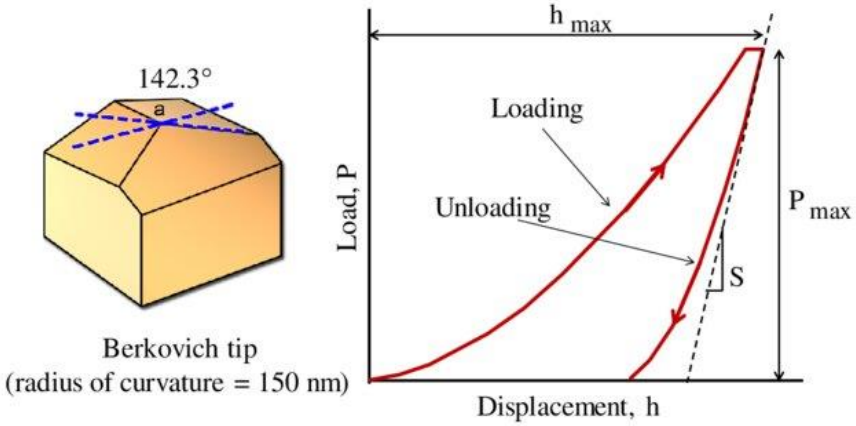


Figure 2-8. Schematic drawing showing the details of Berkovich tip and sample load-displacement curve.


Figure 2-9. Figure of specimens fabricated according to blueprint presented in Figure 2-7

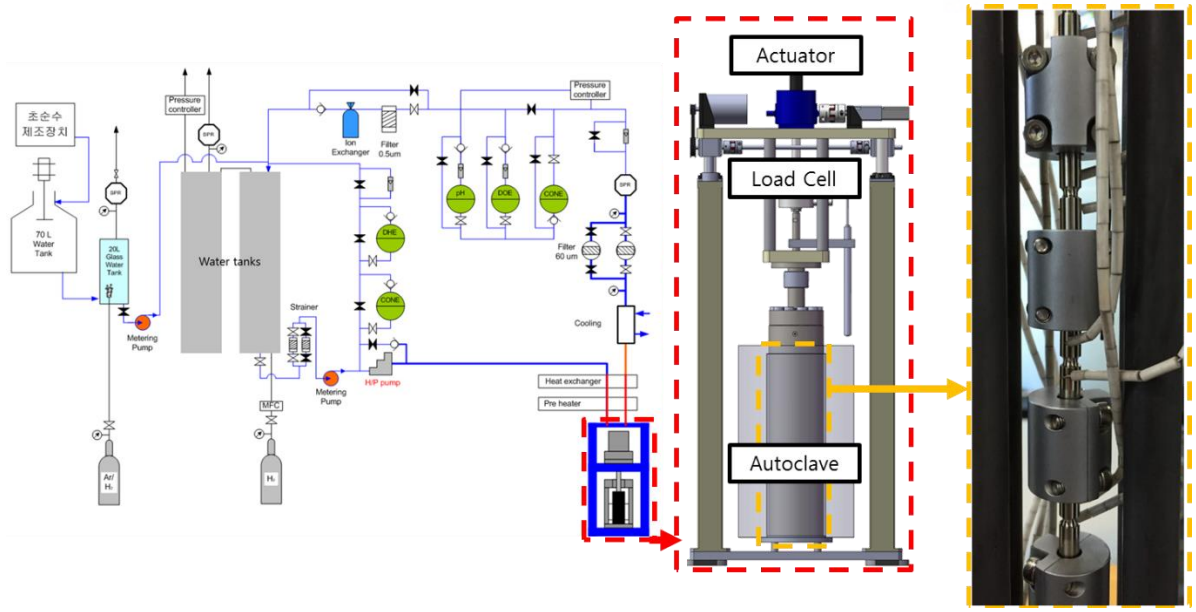


Figure 2-10. Schematics of recirculation loop to simulate PWR primary water environment for SSRT and U-bend test. Right figures show detailed view of autoclave and specimen load train.

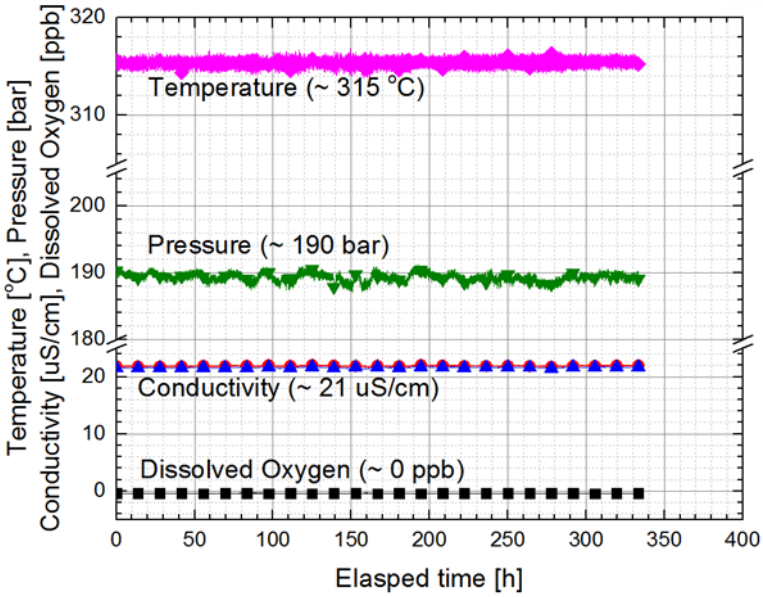


Figure 2-11. Representative graph of temperature, pressure, conductivity and dissolved oxygen concentration acquired by data acquisition system used in this research. Every environmental factor was maintained constantly.

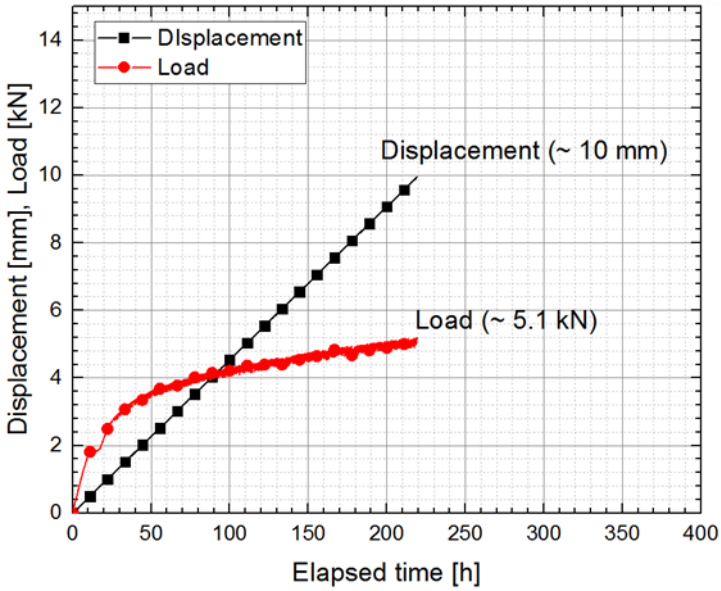


Figure 2-12. Representative graph of displacement and load acquired by data acquisition system used in this research. Every mechanical factor was maintained constantly.

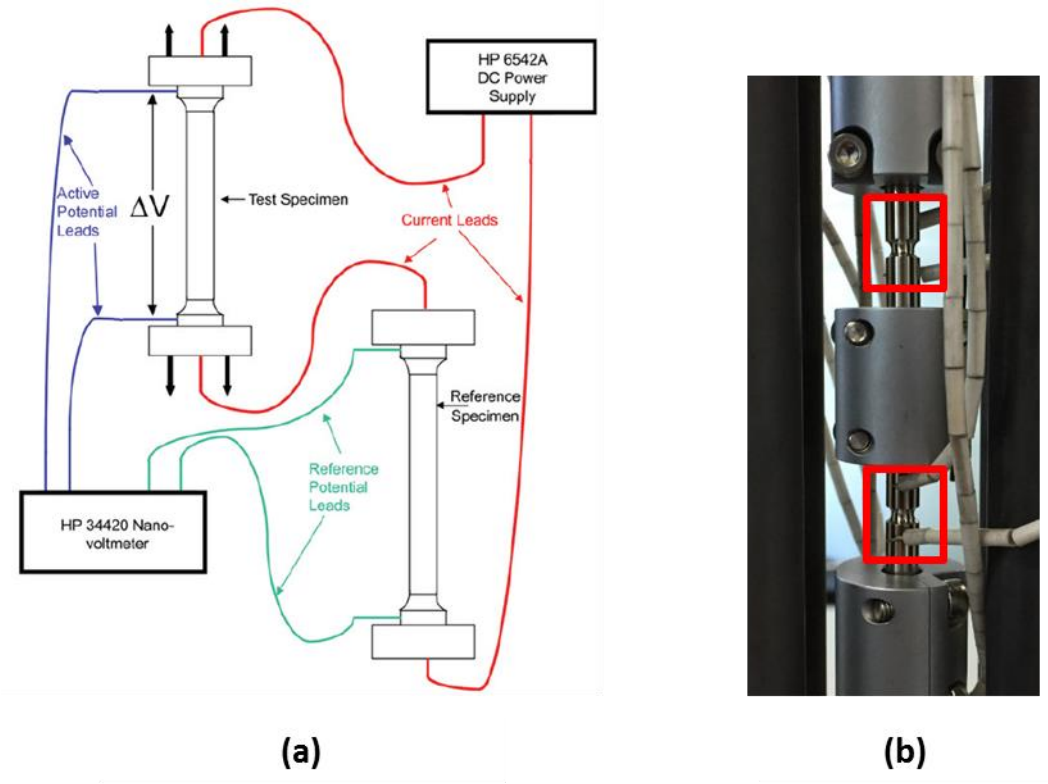


Figure 2-13. (a) Example of wire connection method for DCPD. (b) actual specimen and platinum wire probe for DCPD system [47].

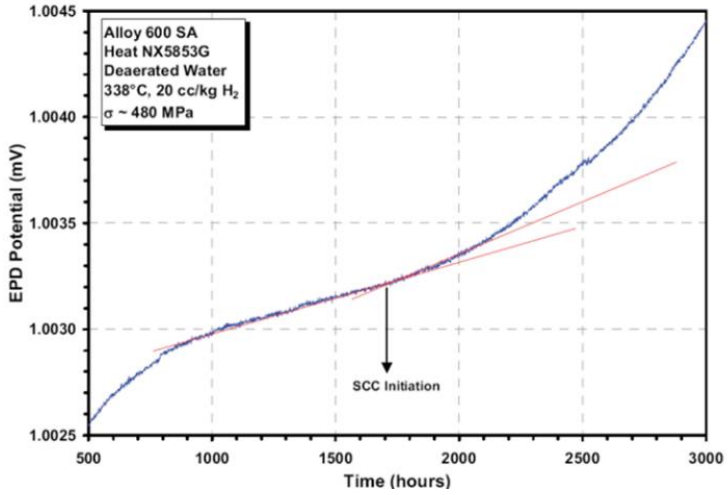


Figure 2-14. Example of crack initiation detect via DCPD method. This researcher decided the crack initiation time as the point of inflection [47].

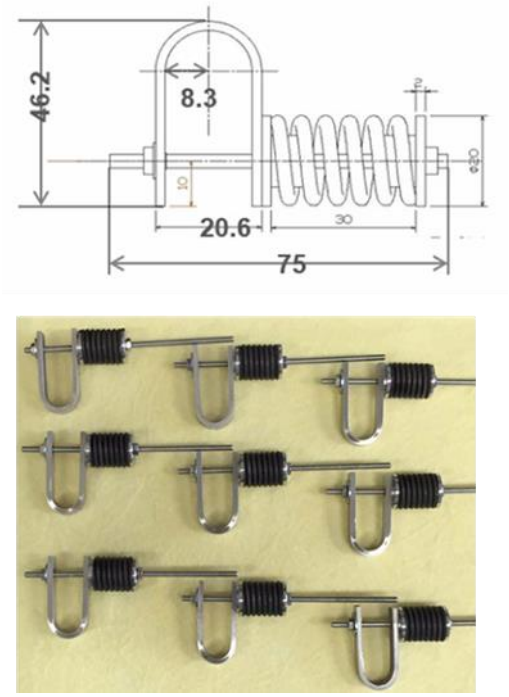


Figure 2-15. Blueprint and actual specimen of U-bend test.

Figure 2-16. Specimen cage used during U-bend test in simulated PWR environment.

# 3. Results

## 3.1. Mechanical properties

Stress strain curve was measured in each specimen and shows in Figure 3-1. Acquired properties are 0.2% offset yield strengths, slope of stress strain curve in early stage (~0.005 mm/mm), elongations and ultimate tensile strengths. Several parameters were deduced from stress strain curves and listed in Table 3-1. The highest yield strength and ultimate tensile strength were observed in 10 years thermally aged specimen. Also due to loss of ductility in 10 years thermally aged specimen, elongation was minimized. It shows that thermal aging evidently effects the mechanical properties of nickel-based alloy. Meanwhile, those hardened in 10 years thermally aged specimen, was softened during 20 years of thermal aging; yield strength and ultimate tensile strength were reduced during 20 years of thermal aging.

Fracture surface of each specimen are summarized in Figure 3-2. Typical ductile failure mode with several dimples were observed in every specimen, however, no sign of severe difference was observed. Since the size and depth of dimples were not unique, it was difficult to quantify the size of it. However, averaged dimple size was relatively large in 10 years thermally aged specimen compared to that of other specimens. This may be the evident of lower ductility of 10 years thermally aged specimen [49], [50]. Meanwhile, at thermally aged specimens, mark of intergranular fracture was observed. It could be caused by the embrittlement due to precipitates formed along grain boundary. These phenomena then induce intergranular fractures which are observed in fracture surface [27].

To investigate the mechanical behavior in micro and nanoscale, nanoindentation was conducted for whole thermally aged specimen. Same trend with tensile test was observed in the results of nanoindentation; hardening during 10 years of thermal aging and softening during 20 years of thermal aging as shown in Figure 3-3. Detailed properties are summarized in Table 3-2. Hardness at grain boundary and grain matrix were almost same, their difference was within error range. This means that precipitates were distributed uniformly along grain boundaries and influence to nanoindentation results uniformly whether it is tested on the grain or grain boundary [51]. Plastic deformation zone often considered to 5 times larger than indentation depth during nanoindentation. Since indentation depth was 2 μm, plastic deformation should be considered as 10 μm, which is large enough to cover several number of precipitates in one indentation in grain matrix or grain boundary [52].

No sign of matrix hardening was observed in both tensile test and nanoindentation test. The matrix could be hardened by the dislocation clusters or increased dislocation density. Those could be detected from the nanoindentation results at matrix of specimen. From the previous researches conducted with nanoindentation [51], ‘pop-in’ phenomenon should be observed at early stage of displacement into

surface – Load graph. However, as shown in Figure 3-3, no sign of dislocation pop-in was observed. This indicate that the density of dislocation might not be increased during thermal aging.

## 3.2. Microstructure

Average grain size of each specimen was measured via SEM and EBSD analysis. It was 26.7 μm at as received specimen, 24.6 μm at 10 years thermally aged specimen and 25.4 μm at 20 years thermally aged specimen. Grain size of specimen were not much changed during thermal aging, since thermal aging temperature used were too low to cause increment of grain size.

Morphology of precipitates were investigated in as received and thermally aged specimen as presented in Figure 3-4. Detailed microstructural features were analyzed with image analyzer. In grain matrix, no significant changes were observed. Most of the precipitates were TiN or NbC which should be formed during mill annealing state, since those could not be formed during thermal aging at 400 ℃, thermodynamically. Therefore, the effect of those TiN or NbC precipitates were not significantly considered in this study. Meanwhile, the number fraction of precipitates in grain boundary was dramatically changed during thermal aging.

Precipitates were originally existed in the grain boundaries of as received specimen. The average length of precipitates was about 0.801 μm, area fraction of it was 0.36 % and length fraction of precipitate to grain boundary was about 19.59 %. During 10 years of thermal aging, the size of precipitates was not changed, however, the number fraction of it was significantly increased. The average length of precipitates was about 0.923 μm, area fraction was 1.20 % and length fraction was 45.17 %. Meanwhile, during 20 years of thermal aging, severe increment was occurred in length of precipitates, and number fraction of it was almost maintained. The average length of precipitates was 1.864 μm, area fraction of it was 1.43 % and length fraction was 48.18 %. As a brief summary, it could be thought that precipitates were formed during 10 years of thermal aging and growth or combine.

Similar result was observed in other studies with nickel-based alloys. In dissimilar metal weld composed of Alloy 152 and low alloy steel A533 Gr. B, precipitate morphology change was observed in both weld metal Alloy 152 and fusion boundary between Alloy 152 and low alloy steel. Precipitates were formed during early stage of thermal aging, also hardening was observed in this period. And there were merely coarsened or migrate to thermodynamically stable position with time [27], [53]–[55].

Chemical composition was investigated with EDS attached SEM and presented in Figure 3-5. (a), (d) and (g) show the region where EDS analysis was conducted. Line profile was performed in two different lines; one was measured from the grain boundaries with precipitates, and the other was

measured from the grain boundaries without precipitates. From the result, precipitates were composed of chromium, detailed analysis was conducted with TEM. Chromium depletion was frequently reported in nickel-based alloy after heat treatment. However, no sign of depletion was observed in this study, as shown in Figure 3-5 (b, e, h). Also, no chromium depletion was observed near chromium carbide as shown in Figure 3-5 (c, f, i). This might be caused by the fact that thermal aging temperature conducted in this study was too low to cause any depletion.

Precipitates were precisely investigated with TEM. Figure 3-6 (a-c) presents dark-field images of each specimens. And Figure 3-6 (g-i) shows EDS results of precipitates. From the two results, precipitates were acknowledged as chromium carbides, specifically $Cr_7C_3$ from the diffraction pattern analysis presented in Figure 3-6 (d-f). Carbides could be formed during heat treatment, since the carbon solubility is very low in austenite structure. Also, several previous studies reported that mostly $Cr_7C_3$ or $Cr_{23}C_6$ are precipitated in grain boundaries [13], [27], [53]. Figure 3-7 shows dislocation morphology at thermally aged specimens. From image analysis, the dislocation density of every specimen was inferred. Density of thermally aged specimens was not changed during thermal aging; as received specimen have 35.3 #/$\mu m^2$, 10 years thermally aged specimen have 31.4 #/$\mu m^2$ and 20 years thermally aged specimen have 35.9 #/$\mu m^2$. It is hard to know the actual dislocation density of specimen with one TEM image, however, it could be explained with the results of nanoindentation where no sign of indentation pop-in was observed. Also, similar evidence was observed in EBSD analysis which will be explained in below paragraph, and this could be reasonable since the samples were not be cold-worked or hardened with any mechanical processes.

EBSD analysis results are summarized in Figure 3-8 and Figure 3-9. Figure 3-8 (a-c) shows the results of grain boundary misorientation analysis based on coincidence site lattice (CSL) theory. CSL boundaries are one of grain boundary types such as low-angle grain boundary (2–15°) and high-angle grain boundaries (over 15°). CSL boundaries are defined by Brandon's criterion $\Delta\theta = 15° \Sigma^{-0.5}$, where $\Delta\theta$ is the angular deviation from the exact CSL boundary and $\Sigma$ is the reciprocal of CSL [56]–[59]. CSL boundaries are classified by $\Sigma$ number from 3 to 59, however, only $\Sigma$ numbers below 19 were counted in this study, because those boundaries are known to have special material degradation characteristics including high corrosion or precipitation resistance [57]. CSL boundaries, low-angle grain boundaries and high angle grain boundaries were marked with red, green and black color, respectively. The CSL boundary fraction of as received, 10 years thermally aged and 20 years thermally aged specimen were 38.4 %, 33.0 % and 36.9 %. Most of CSL boundaries were $\Sigma$ 3 boundaries, and this is coincidence result with previous studies. [60], [61]. However, the fraction of CSL boundaries were almost not changed during thermal aging. In general, CSL boundaries are known to be increased during heat treatment, however, in this research, too low temperature might prevent the formation of CSL boundaries during thermal aging [61]. Figure 3-8 (d-f) represent the kernel

average misorientation (KAM) which is proportional to local residual strain distribution caused by inhomogeneous dislocation distribution [62]. As shown in figure, no significant change was observed. It could be coincidence results of those conducted to reveal the dislocation density, since KAM could be increased by increment of dislocation density.

High resolution EBSD was conducted to reveal the correlation between grain orientation and carbide orientation. As shown in Figure 3-9, $Cr_7C_3$ and grain matrix have different crystallographic structure; $Cr_7C_3$ have trigonal structure while matrix have cubic structure. Therefore, precipitates were not growing toward matrix, but growing toward grain boundary direction as shown in figure. Several researchers reported that carbides often grow toward matrix, but the precipitates they observe was Cr23C6 in Alloy 690 which have cubic structure which could have coherency with grain matrix [12], [63]. Also as shown in figure, carbides were formed majorly on high-angle grain boundary while those were not be formed on CSL boundaries.

## 3.3. Corrosion resistance

Cross section of specimen after immersion corrosion test according to ASTM A262 practice C is shown in Figure 3-10. The weight loss rates obtained were 5.04 mm/yr for as received, 6.97 mm/yr for 10 years thermally aged specimen, and 5.23 mm/yr for 20 years thermally aged specimen. Intergranular corrosion was observed in as received and thermally aged specimen and it was most severe in 10 years thermally aged specimen. From this results, it could be thought that 10 years thermally aged specimen have the most significant galvanic effect between carbide and grain boundary or matrix since no sign of chromium depletion was observed during EDS analysis in every specimen [12], [64].

Results graphs of potentiodynamic electropolarization are shown in Figure 3-11. The corrosion potential of each specimen was measured: -401 mV for as received, -409 mV for 10 years thermally aged specimen, and -446 mV for 20 years thermally aged specimen versus the SHE. In addition, the corrosion current densities of each specimen were 0.131, 0.0902, and 0.141 $\mu A/cm^2$ for as received, 10 years thermally aged specimen, and 20 years thermally aged specimen, respectively. A slight transition of active-passive region was observed in 20 years thermally aged specimen, while this phenomenon was not observed in as received and 10 years thermally aged specimen. However, no significant difference was observed in corrosion potential or corrosion current density: might be caused by the fact that polarization covers somewhat large area while changes caused by thermal aging is limited to small area [65]–[68].

Oxide layer of thermally aged specimens were investigated with SEM. Oxide layers were formed by immersion samples at simulated primary water environment for 750 h. As shown in Figure 3-12,

square or round shape of oxides were observed; which was Ni-Fe spinels. Also needle-like NiO spinels were observed. However, those were not changed during thermal aging as shown in figure. Thermal aging temperature or changes induced by thermal aging might have little effect in terms of oxidation in primary circuit environment.

## 3.4. SCC susceptibility

SSRT was used to investigate the SCC susceptibilities of as received and thermally aged Alloy 600. DCPD graphs are shown in Figure 3-13. At the DCPD curve, point of inflection at 3$^{rd}$ polynomial fitting was defined as SCC initiation time. Loop conditioning and pressure fluctuations causes electronic noise, however, gradient change and point of inflection was clearly observed in every graphs of Figure 3-13. The highest susceptibility to PWSCC initiation was observed in the results of 10 years thermally aged specimen, having the shortest SCC initiation time of 432.8 ± 33.4 h, and 20 years thermally aged specimen and as received exhibited longer times by having SCC initiation of 556.9 ± 36.5 h and 585.9 ± 13.8 h, respectively. Specimen surfaces were investigated after SCC initiation to analyze the cracking mode. Multiple cracks were observed which have approximately 30 μm length in every crack-initiated specimen. The shape of cracks were zigzag shape along the grain boundaries as shown in Figure 3-14, and those were acknowledged as cracks formed by SCC. Also previous studies reports same trend that the SCC are generally propagates as intergranular cracking [17]–[19], [69]–[71].

Different aspects with smooth specimen was observed with the specimens with triaxial stress applied. PWSCC susceptibility was almost similar for 10 years thermally aged specimen and 20 years thermally aged specimen and as received shows the lowest PWSCC susceptibility as shown in Figure 3-15. Representative surface crack morphology is shown in Figure 3-16. No significant difference was observed in the surface morphology of both specimens.

Table 3-1. Mechanical properties achieved from tensile tests of thermally aged specimens

| Specimen | | As received | HT400_Y10 | HT400_Y20 |
|---|---|---|---|---|
| Slope of early stage deformation [GPa] | 25 ℃ | 211.3 ± 12.0 | 290.7 ± 11.9 | 256.7 ± 46.4 |
| | 325 ℃ | 188.9 ± 2.4 | 157.2 ± 6.6 | 167.9 ± 11.1 |
| 0.2 % offset yield strength [MPa] | 25 ℃ | 409.5 ± 10.9 | 587.3 ± 5.9 | 497.3 ± 2.2 |
| | 325 ℃ | 409.7 ± 50.5 | 433.7 ± 81.8 | 473.6 ± 116.3 |
| Ultimate tensile strength [MPa] | 25 ℃ | 701.8 ± 24.5 | 775.7 ± 24.7 | 767.7 ± 2.5 |
| | 325 ℃ | 666.7 ± 10.7 | 675.1 ± 35.3 | 673.6 ± 12.4 |
| Elongation [%] | 25 ℃ | 50.0 ± 1.6 | 36.0 ± 1.6 | 42.0 ± 3.1 |
| | 325 ℃ | 40.7 ± 3.7 | 38.7 ± 9.2 | 38.1 ± 6.8 |

Table 3-2. Nanoindentation hardness achieved from nanoindentation test

| Investigated location | As received | HT400_Y10 | HT400_Y20 |
|---|---|---|---|
| Inside grain [GPa] | 2.44 ± 0.03 | 2.75 ± 0.08 | 2.55 ± 0.09 |
| Cover grain boundary [GPa] | 2.5 ± 0.02 | 2.76 ± 0.05 | 2.6 ± 0.1 |
| Average hardness [GPa] | 2.47 ± 0.14 | 2.81 ± 0.24 | 2.59 ± 0.31 |

Table 3-3. Microstructural and orientation characteristics of specimens

| Specimen | As received | HT400_Y10 | HT400_Y20 |
|---|---|---|---|
| Area fraction of precipitates [%] | 0.36 ± 0.04 | 1.2 ± 0.1 | 1.43 ± 0.14 |
| Length fraction of precipitates at grain boundary [%] | 19.59 ± 3.4 | 45.17 ± 4.1 | 48.18 ± 3.7 |
| Precipitate length [μm] | 0.80 ± 0.30 | 0.92 ± 0.31 | 1.86 ± 1.19 |
| Spacing between precipitates [μm] | 2.78 ± 0.22 | 1.92 ± 0.14 | 3.28 ± 0.31 |
| Grain size [μm] | 26.67 ± 0.15 | 24.61 ± 0.21 | 25.39 ± 0.25 |
| Kernel average misorientation [°] | 0.653 ± 0.083 | 0.536 ± 0.074 | 0.701 ± 0.081 |
| Fraction of CSL boundary [%] | 38.4 ± 0.8 | 33.0 ± 0.88 | 36.9 ± 0.41 |

Table 3-4. SCC initiation times measured in this study

| Specimen type | | SCC initiation time [h] | | |
|---|---|---|---|---|
| | | As received | HT400_Y10 | HT400_Y20 |
| Smooth specimen | 315 ℃ | 585.9 ± 13.8 | 432.8 ± 33.4 | 556.9 ± 36.5 |
| | 340 ℃ | 304.8 ± 3.0 | 241.5 ± 16.2 | 293.5 ± 14.1 |
| U-bend test | 325 ℃ | 1125 ± 129.9 | 850 ± 50 | 1125 ± 129.9 |
| | 350 ℃ | 700 ± 141.4 | 650 ± 50 | 700 ± 141.4 |
| Notched specimen | 315 ℃ | 307.1 ± 16.1 | 253.1 ± 6.3 | 205.8 ± 0.3 |
| | 340 ℃ | 179.4 ± 9.9 | 166.6 ± 17.3 | 157.4 ± 12.2 |

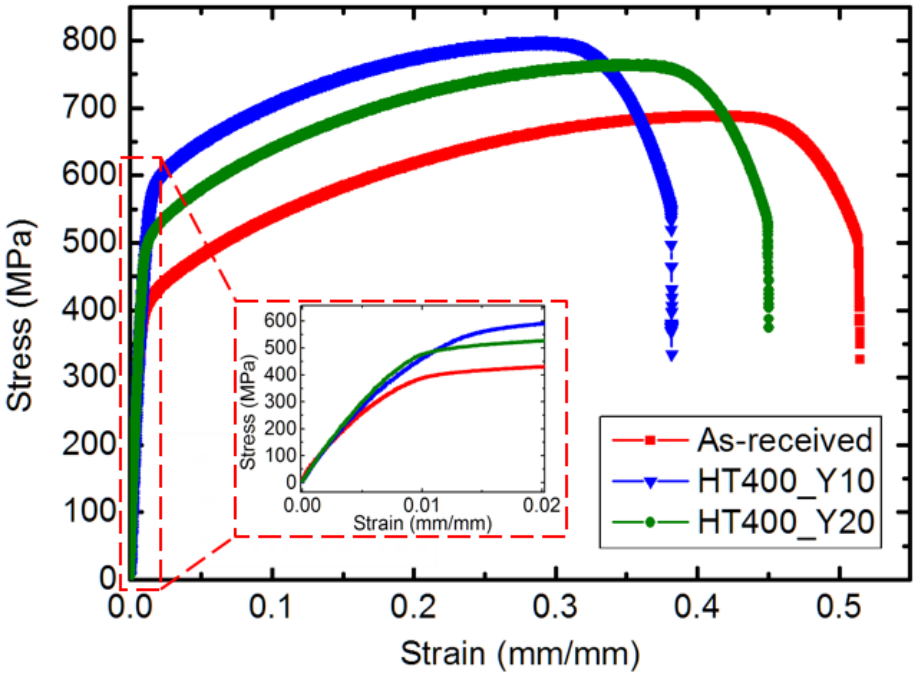


Figure 3-1. Stress-strain curves of the thermally aged specimens. Small graph shows magnified scale at early stage of stress-strain curve. Only representative graph is shown in the figure to propose the shape of graph. Detailed data are summarized in Table 3-1.

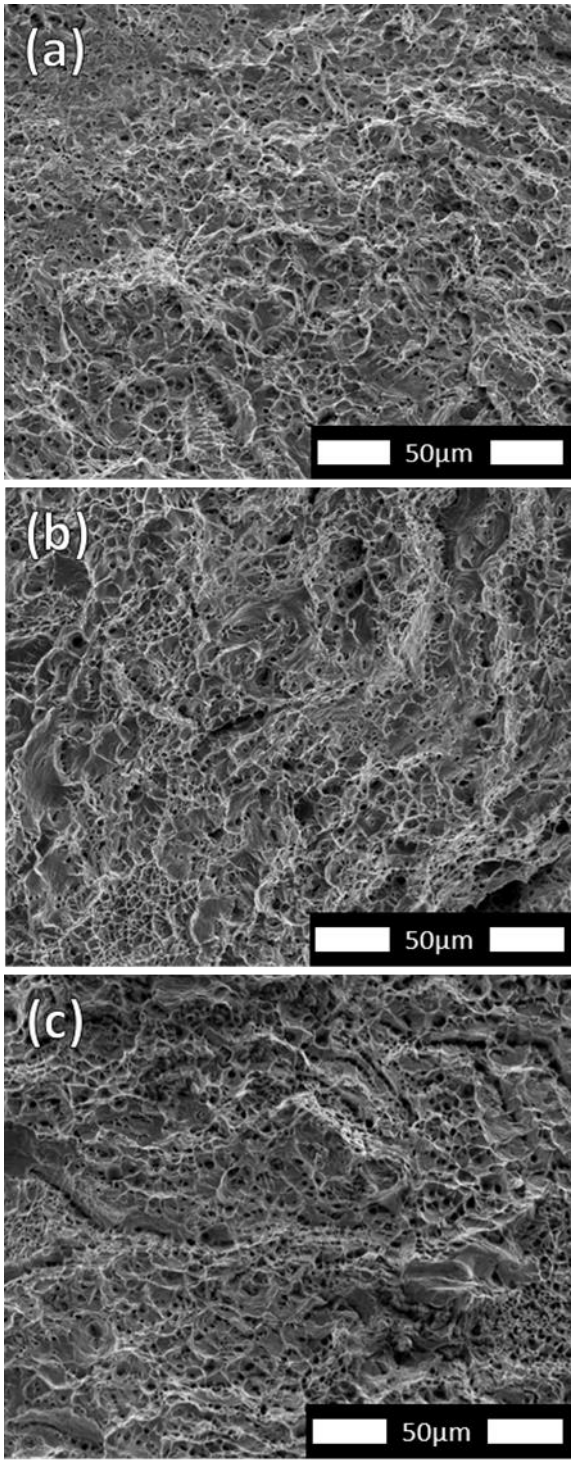


Figure 3-2. Fracture surfaces after test result at room temperature, (a) as received, (b) 10 years thermally aged specimen and (c) 20 years thermally aged specimen. Detail results are summarized in Table 3-3.

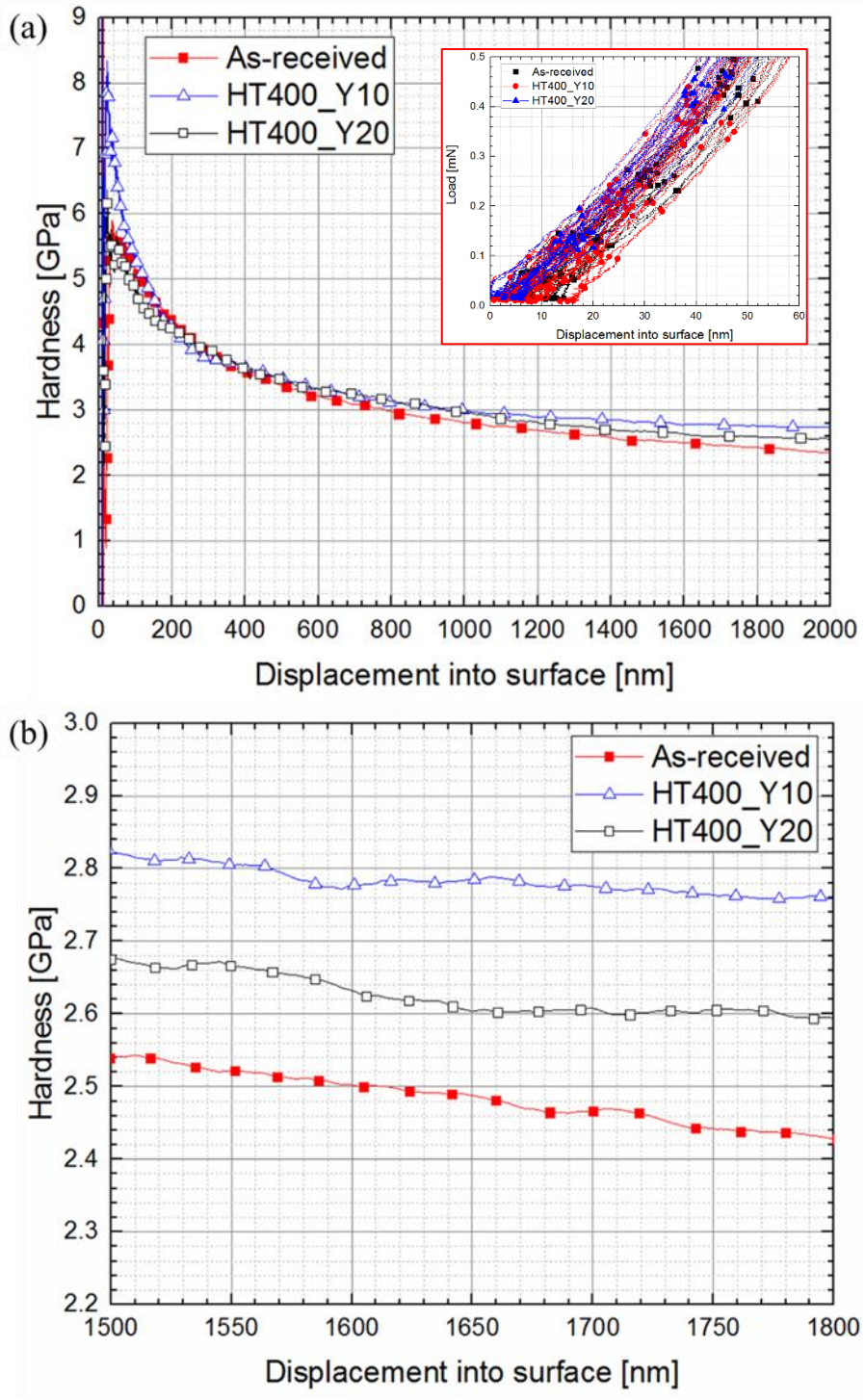


Figure 3-3. Nanoindentation results of each specimen. (a) shows full curve of displacement into surface and hardness. Magnified scale at early stage indentation is also inserted upper side of figure. (b) represents magnified graph of (a) in the range from 1500 nm to 1800 nm. Only representative graph is shown in the figure to propose the shape of graph. Detailed data are summarized in Table 3-2.

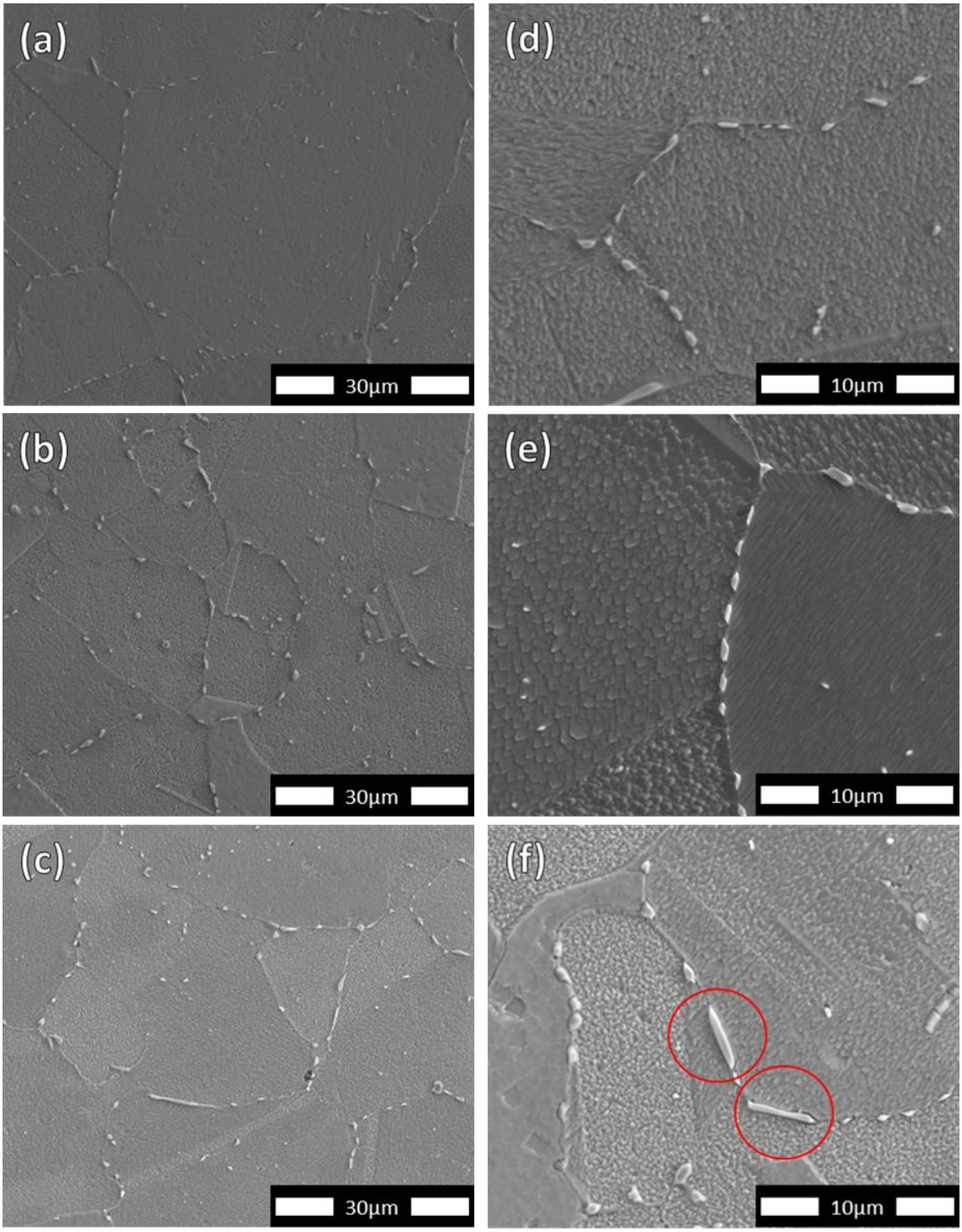


Figure 3-4. SEM images of (a, d) as received, (b, e) 10 years thermally aged and (c, f) 20 years thermally aged specimen. (d, e, f) are the magnified images of each specimen.

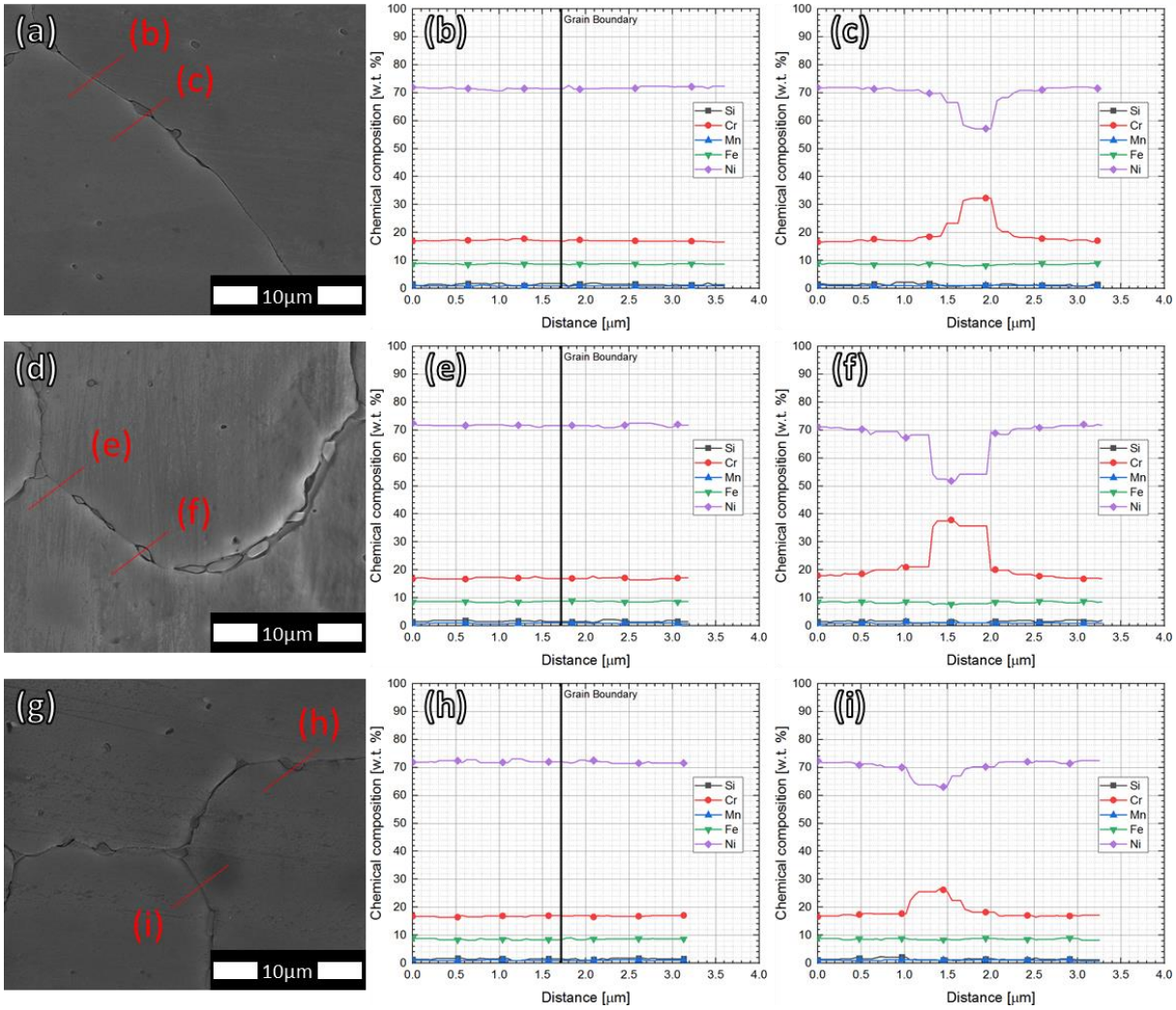


Figure 3-5. EDS analysis results of as received (a, d, g), 10 years thermally aged (b, e, h) and 20 years thermally aged (c, f, i). (a, d, g) present the line location where EDS analysis were done. And (b, e, h) show analysis results at grain boundaries without precipitate. (c, f, i) are the results measured at grain boundaries with precipitate.

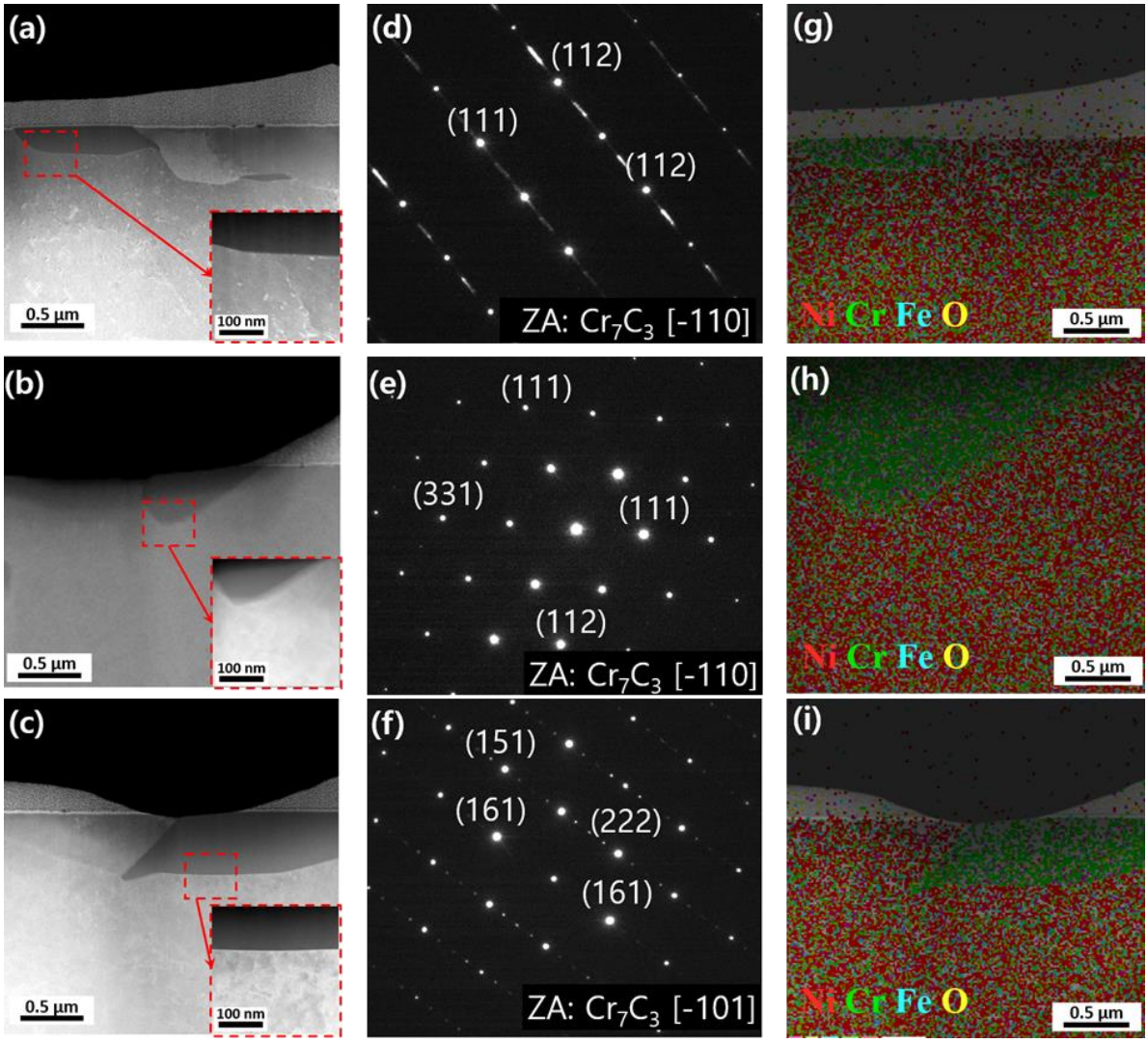


Figure 3-6. TEM analysis results of as received (a, d, g), 10 years thermally aged (b, e, h) and 20 years thermally aged (c, f, i) specimen. (a, b, c) show Dark-field TEM images of precipitates, (d, e, f) shows diffraction pattern analyzed at the marked region with red box. (g, h, i) represent EDS result of each specimen.

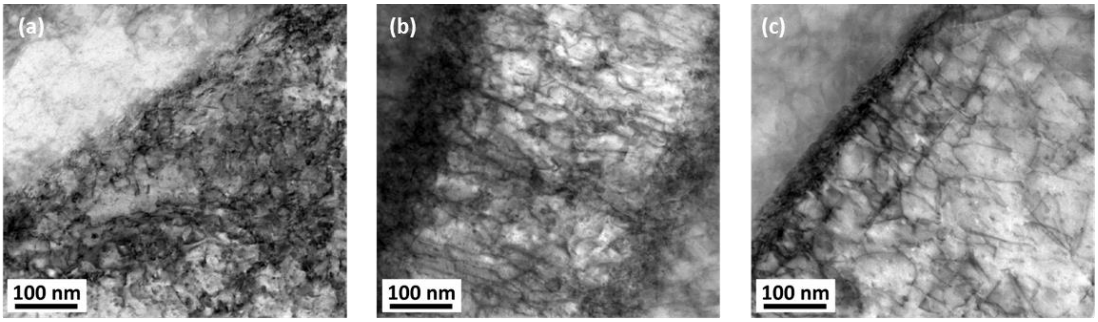


Figure 3-7. Dislocation density analysis of (a) as received, (b) 10 years thermally aged specimen and (c) 20 years of thermally aged specimen. Dislocation density of specimens were not increased during thermal aging.

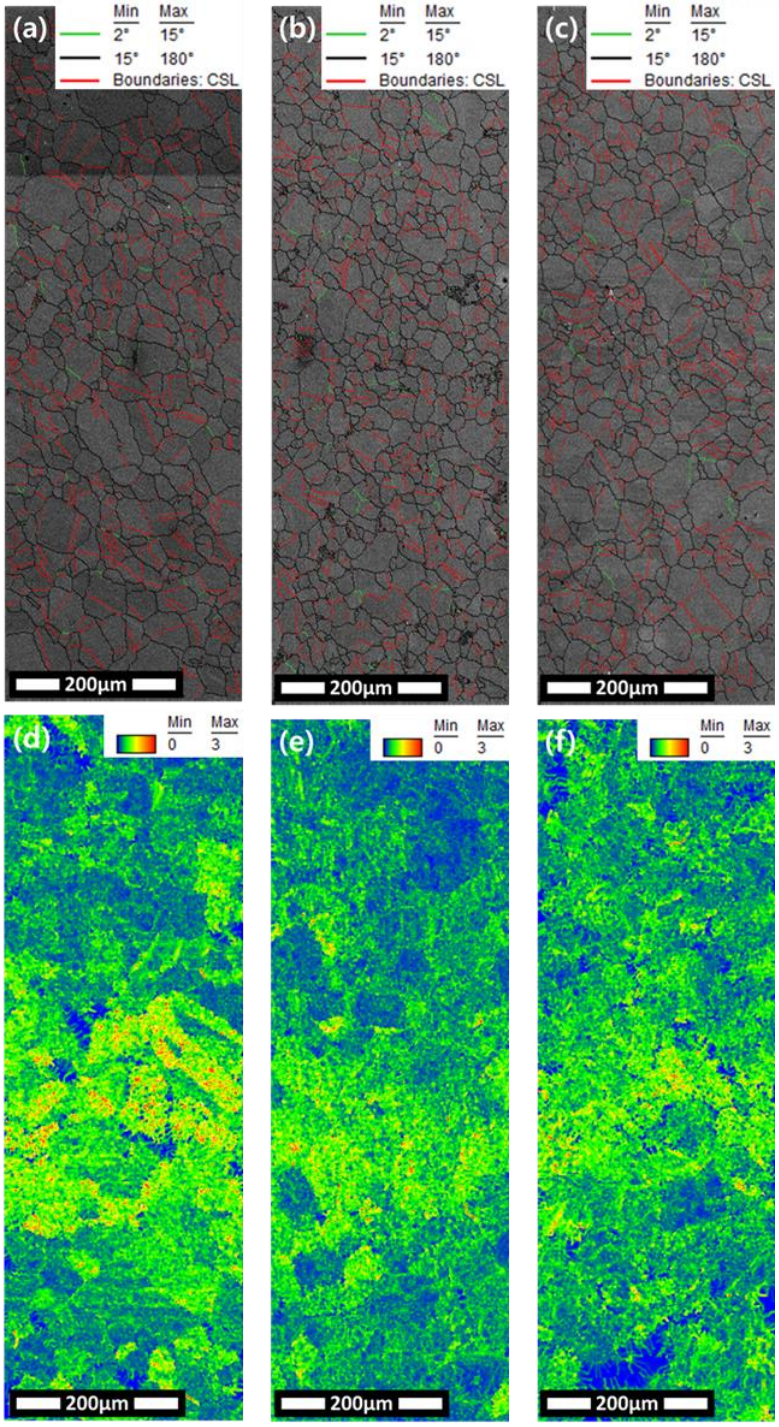


Figure 3-8. EBSD analysis results of (a, d) as received, (b, e) 10 years of thermally aged specimen and (c, f) 20 years of thermally aged specimen. Coincidence site lattice boundaries are marked with red color, low angle grain boundaries are marked with green color and high angle grain boundaries are marked with blue color in (a), (b) and (c). Kernel average misorientation is represented in (d), (e) and (f).

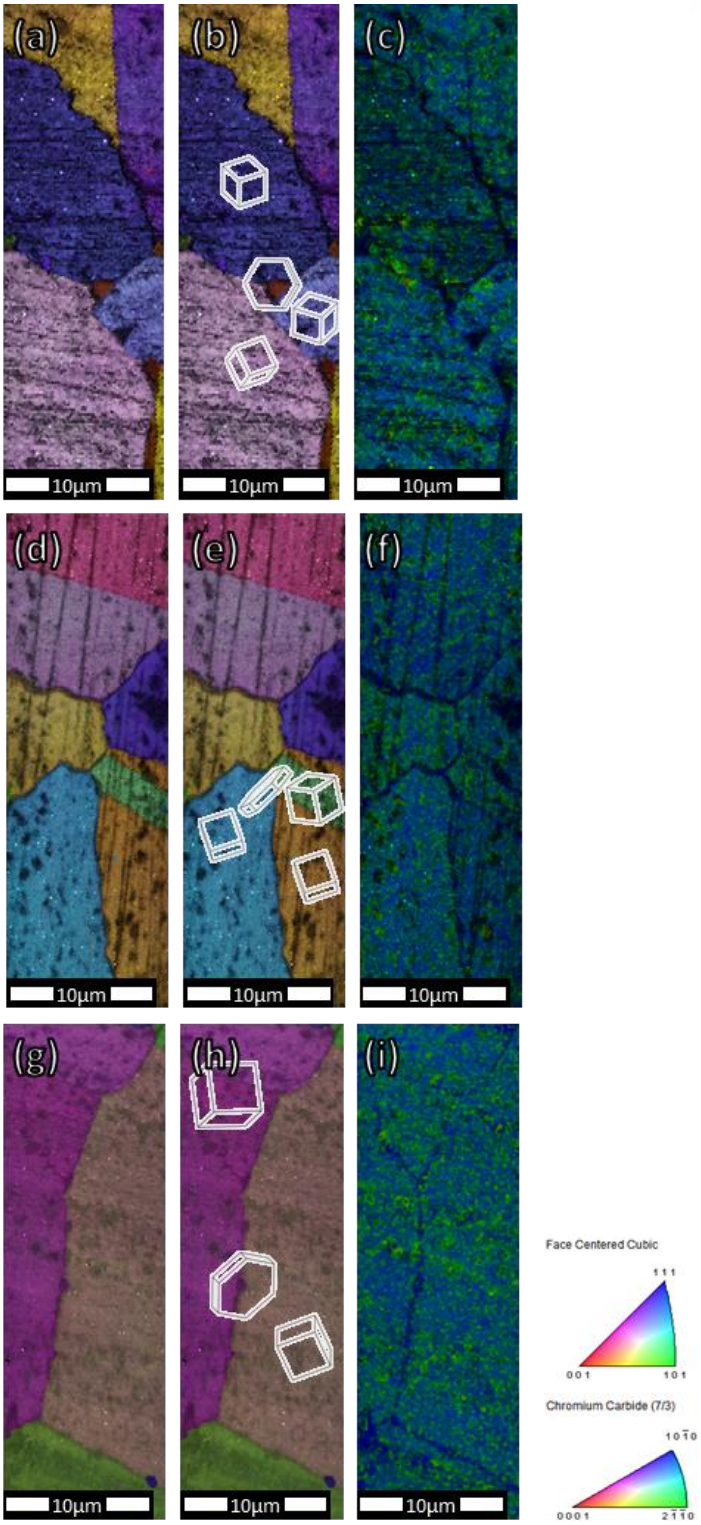


Figure 3-9. High resolution EBSD analysis results. (a), (d) and (g) show inverse pole figure map of as received, 10 years thermally aged and 20 years thermally aged specimen, respectively. And crystal orientation of precipitate and near grains is marked at (b) as received, (e) 10 years thermally aged and (h) 20 years thermally aged. And (c), (f) and (i) are show kernel average misorientation of as received, 10 years thermally aged and 20 years thermally aged specimen, respectively.

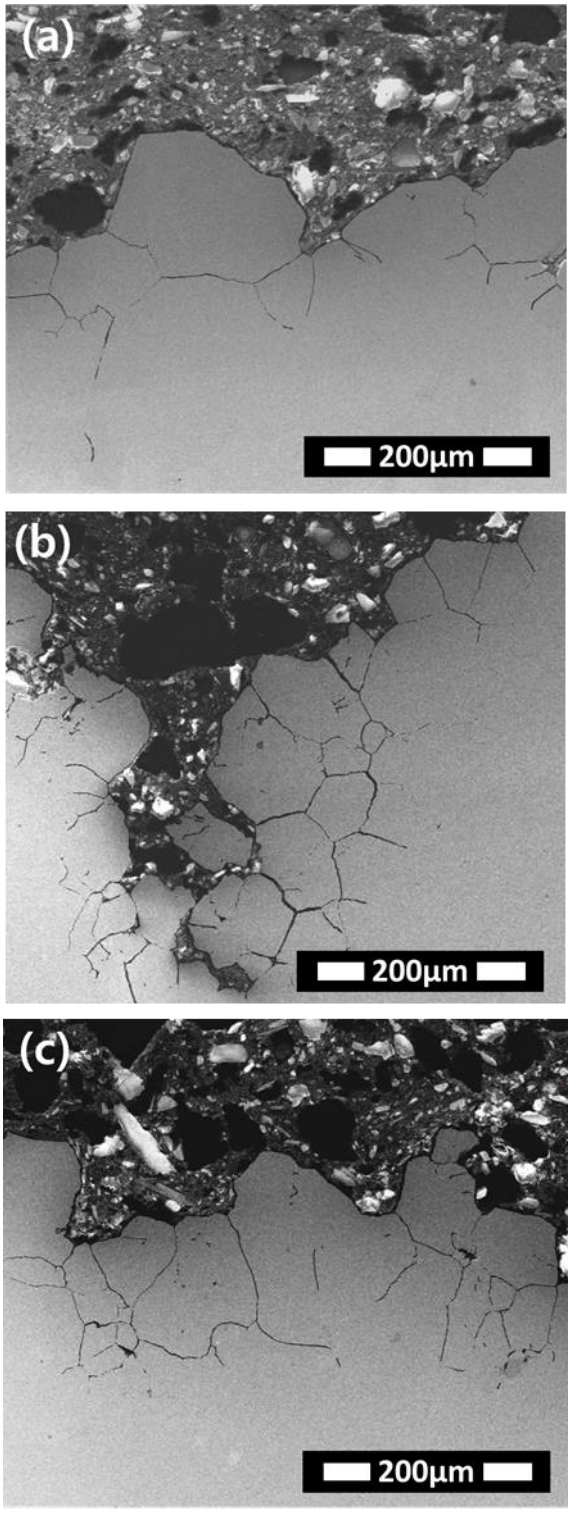


Figure 3-10. Cross section of specimen after immersion corrosion test according to ASTM A262 practice C, (a) as received, (b) 10 years thermally aged and (c) 20 years thermally aged specimen.

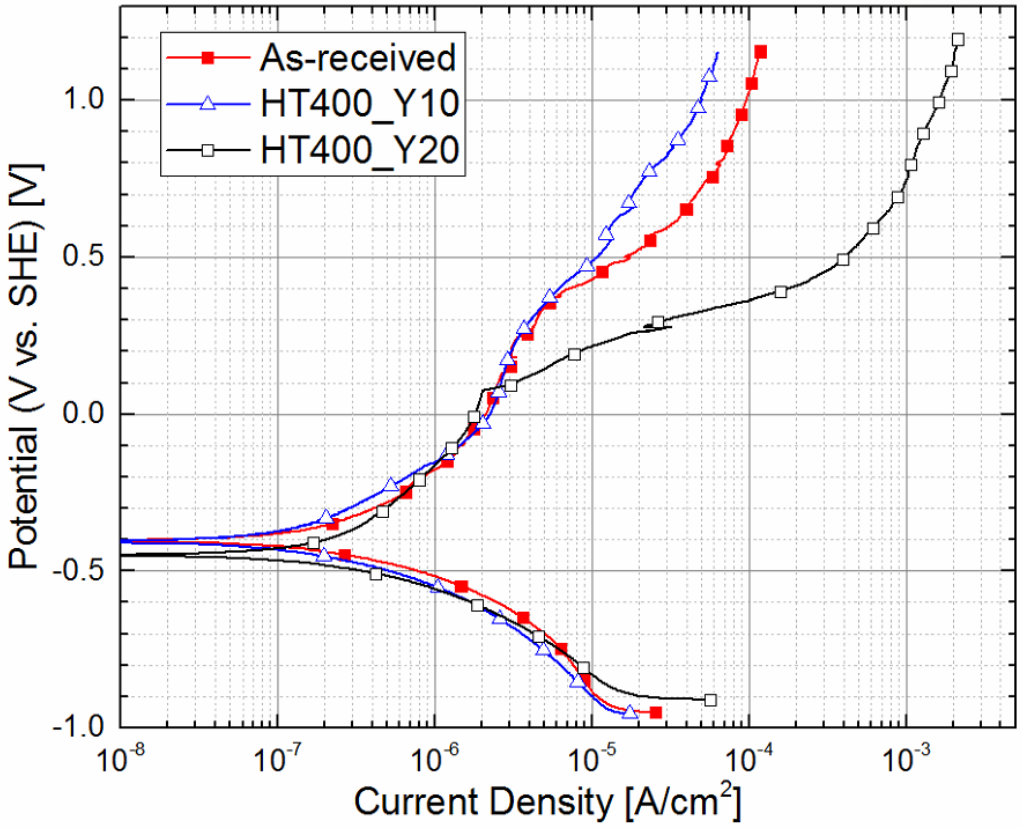


Figure 3-11. Potentiodynamic polarization curves of each specimen. Different colors and symbols are representing each result. Error bar was omitted in this graph for better legibility. Detailed parameters are summarized in Table 3-3.

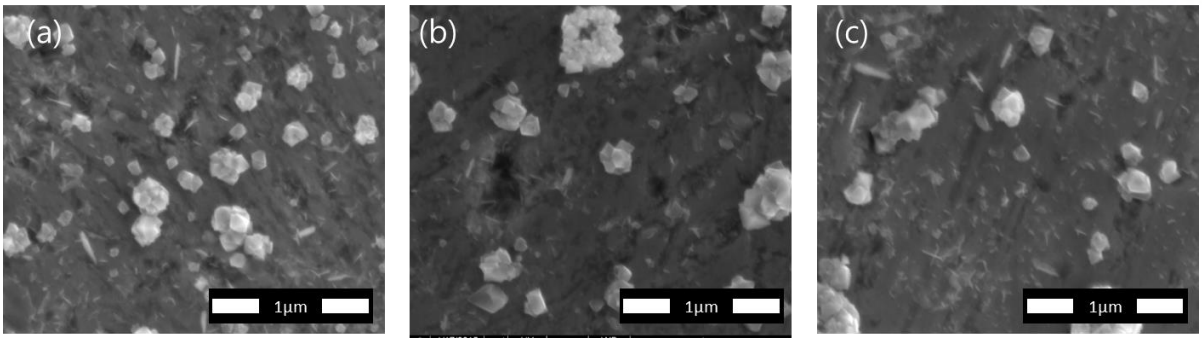


Figure 3-12. Oxide layer of (a) as received, (b) 10 years thermally aged and (c) 20 years thermally aged specimen in simulated PWR water environment for 750 h. There were no significant changes during thermal aging in terms of oxide layer.

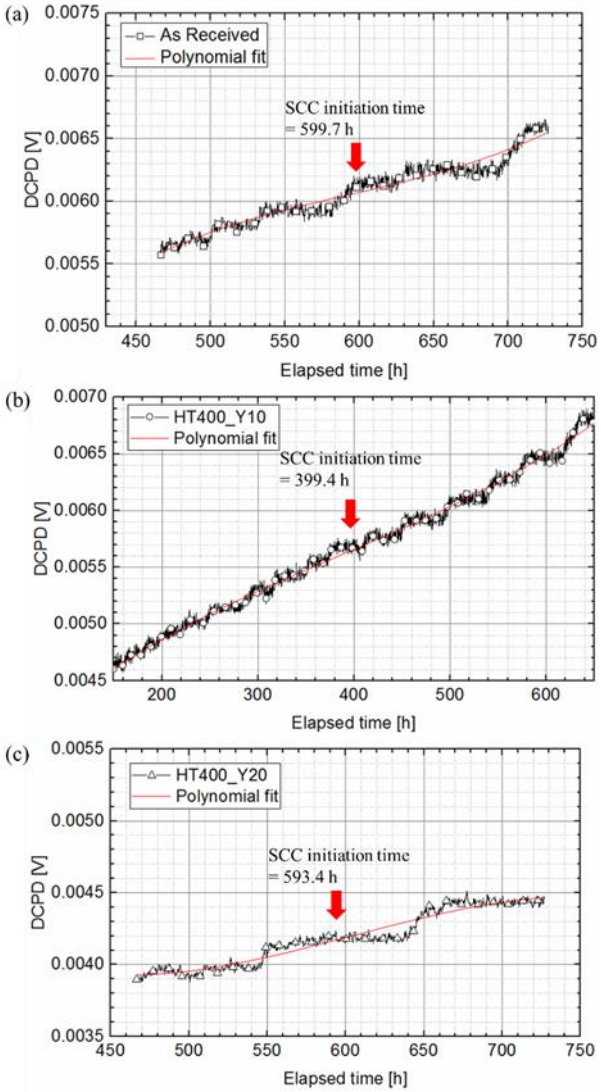


Figure 3-13. Representative DCPD curves observed during SSRT with smooth specimen, (a) as received, (b) 10 years thermally aged and (c) 20 years thermally aged specimen. Point of inflection was clearly observed in all graphs, which were determined as PWSCC initiation time in this study. Note that these results are representative ones from multiple DCPD curves, to show the trend and inflection point of polynomial fitting. Detailed PWSCC initiation time is summarized in Table 3-4.

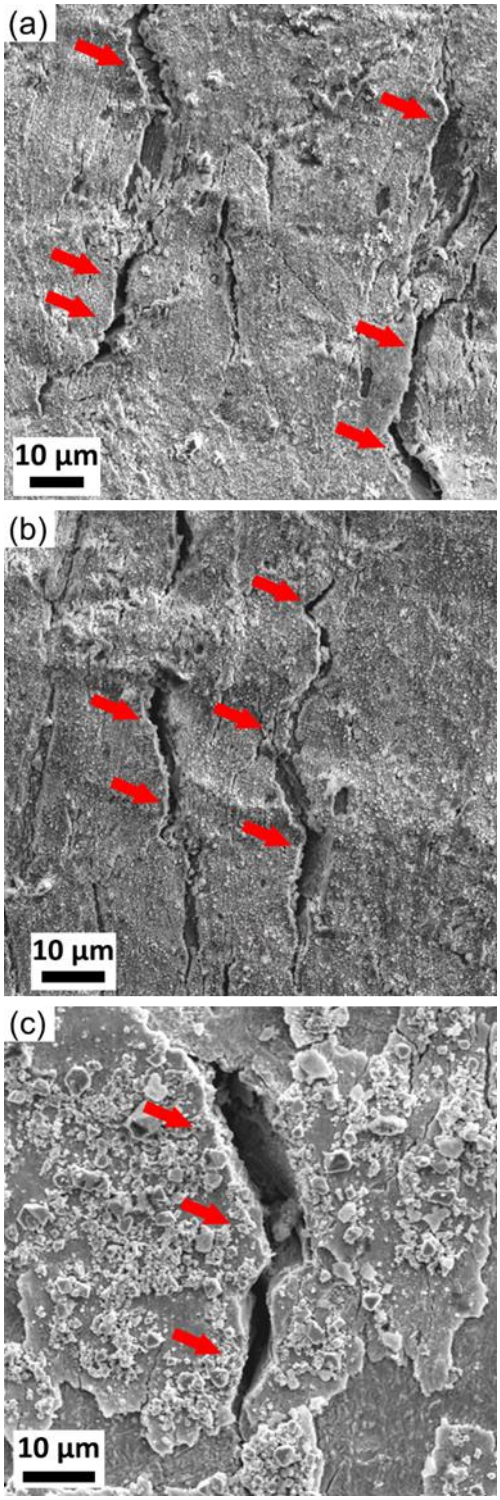


Figure 3-14. Surface analysis results of SCC initiated specimens after SSRT with smooth specimens, (a) as received, (b) 10 years thermally aged and (c) 20 years thermally aged specimen.

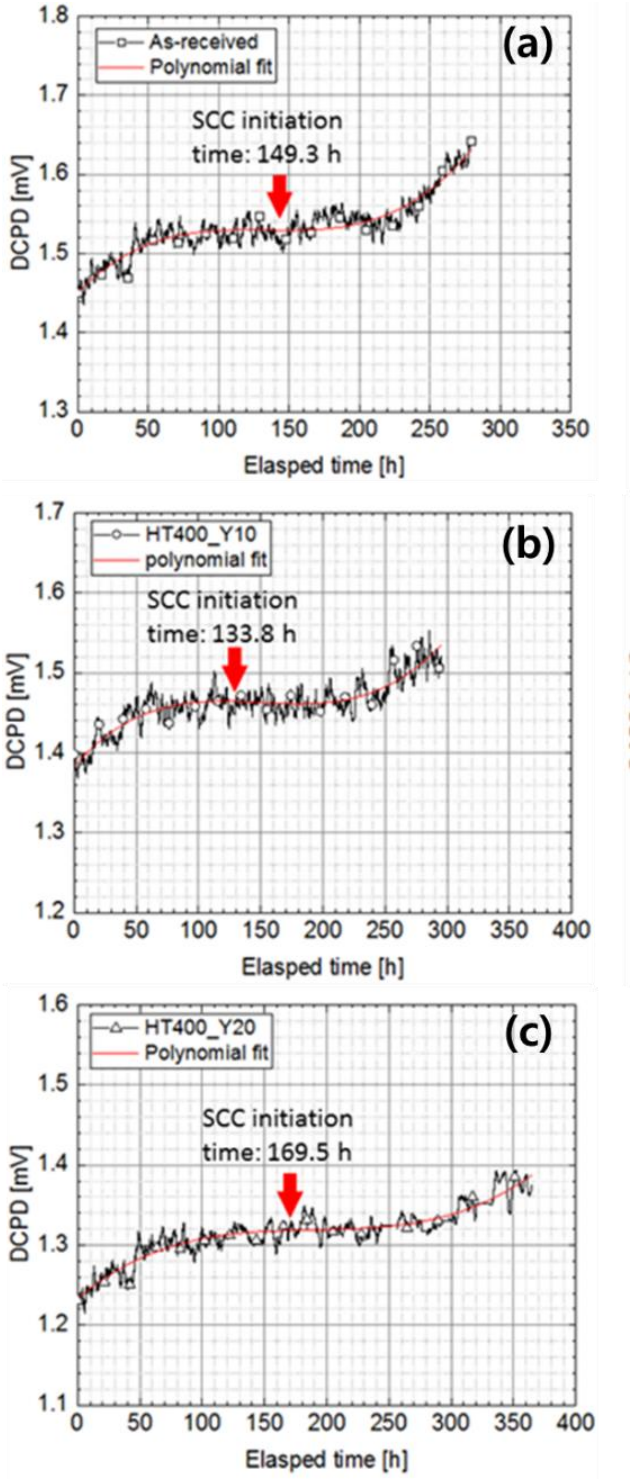


Figure 3-15. Representative DCPD curves observed during SSRT with notched specimen, (a) as received, (b) 10 years thermally aged and (c) 20 years thermally aged specimen. Point of inflection was clearly observed in all graphs, which were determined as PWSCC initiation time in this study. Note that these results are representative ones from multiple DCPD curves, to show the trend and inflection point of polynomial fitting. Detailed PWSCC initiation time is summarized in Table 3-4.

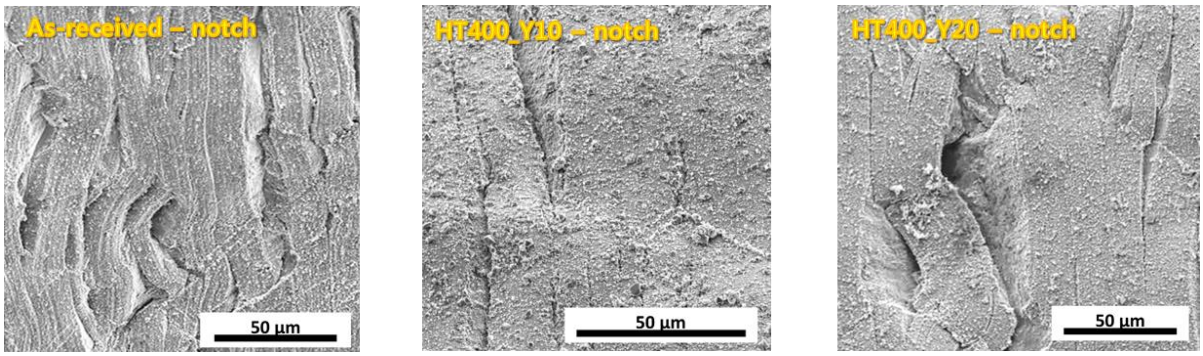


Figure 3-16. Surface analysis results of SCC initiated specimens after SSRT with notched specimens, (a) as received, (b) 10 years thermally aged and (c) 20 years thermally aged specimen.

# 4. Discussion

## 4.1. Hardening and softening behavior

Table 3-3 shows summarized results obtained from microstructural and orientation analysis. As shown in table, 10 years thermally aged specimen exhibit the largest strength due to precipitate hardening. Strength was softened during 20 years of thermal aging which might be caused by increased size of precipitates. Similar trend was observed in the previous study about nickel-based weld metal alloy 152; Alloy 152 was hardened during 15 years of thermal aging, and it was softened by 30 and 60 years of thermal aging [9]. Also, the effect of precipitate was significant in that study. According to other studies, abundance of precipitates could cause increment of tensile properties of material by blunting crack tips or do a role as dislocation sources [54], [72]. During early stage of nanoindentation, the matrix hardening effect might have major effect to material hardening. Matrix could be hardened by dislocation or precipitates in matrix; however, no sign of hardening was observed during early stage of nanoindentation deformation. Also, dislocation density observed with TEM and EBSD shows no change of it. And precipitates in matrix observed with SEM also shows no change during thermal aging. This could be an evident that dislocation or precipitates in matrix was not changed during thermal aging.

Metal hardening or softening due to precipitates were investigated extensively for nickel-based superalloys [23], [73], [74]. Major approach of precipitation hardening is depended on the movement of dislocation across the precipitates; dislocation cut the precipitation or make a loop around it. When the size of precipitate is small, dislocation is cut the precipitate to move across it. However, when the precipitates grow enough, dislocations cannot cut the precipitates, instead they detour the precipitate and leave a loop around it. The hardening effect of this make a loop movement is less noticeable then the cutting [75]–[77]. The critical size between cutting and looping is not defined well depends on the property or characteristics of material [76].

Frequently used equation to explain the amount of hardening due to precipitate is Orowan Mechanism, as shown in the equation below where ($\tau$) is material strength (shear stress to cut or loop around a particle) G is shear modulus, b is the magnitude of Burgers vector, D is distance between pinning particles and r is the radius of precipitate.

$$\tau = \frac{Gb}{D-2r} \qquad (3)$$

Among the parameters, shear modulus and Burger vector was assumed to be constant since every material used in this study was Alloy 600 with or without thermal aging and other precipitate parameters were used with the values in Table 3-3. The calculation result is shown in Figure 4-1. Same trend with that of yield strength was observed; hardening for 10 years and softening during 20 years of thermal aging. From the results, it could be thought that morphology of precipitate is closely related to the mechanical properties [76]–[78].

Meanwhile, Ashby [54] propose a dislocation model that voids and overlaps were occurred near grain boundary while tensile test. To compensate the voids or overlaps, formation of dislocations is induced near the precipitates of grain boundary. Model by Ashby suggest that large number density of precipitates could cause the concentration of stress and dislocations near the precipitates, and cause hardening of the material. During 20 years of thermal aging, length of precipitate is longer than that of 10 years thermally aged or as received, weakening dislocation barrier, finally causing softening [19], [50].

## 4.2. PWSCC initiation of smooth specimen

PWSCC susceptibility also influenced by precipitate morphology. In fact, it could be thought that yield strength is affected by precipitate morphology, and then PWSCC susceptibility is influenced by it. Also, previous researches report that grain boundary precipitates could do a role as sources of major dislocation during deformation at high temperature, which could cause initiation of PWSCC [27], [79]. Relevant results were observed in SSRT conducted with smooth specimen. In addition, intergranular cracking was observed in the surface of PWSCC initiated specimen, same result observed in previous studies; grain boundaries are influenced by precipitation and become brittle or susceptible to PWSCC initiation [25], [80].

Based on the above approach, calculation was conducted to find out the trend of PWSCC susceptibility of smooth specimen. It was found that PWSCC susceptibility is inversely proportional to PWSCC initiation time measured in this study as shown in Figure 4-2. From this result, it could be thought that PWSCC susceptibility under monoaxial stress state could be explained by Orowan mechanism.

Several other possible explanations are suggested by previous studies, since mechanism of SCC is not clarified yet. Long-term thermal aging induces changes of corrosion characteristics such as oxide, which known to influence significantly to SCC susceptibility [81]–[83]. Several researchers report that the chromium protective oxide layer stability could be damaged or unstable owing to chromium depletion in grain boundary, which could increase SCC susceptibility during SSRT [84]. Also, one

possible explanation of PWSCC of nickel-based alloy degraded in high temperature is short-range ordering, however, the mechanism of short-range ordering influencing to PWSCC initiation is not clarified. In addition, heat treatment during 100 – 1000 h at 450–525 ℃ known to cause short-range ordering. Therefore, it could not be formed during thermal aging of this study which 400 ℃, might be insignificant to form ordering. Short-range ordering also known to be formed during deformation at high temperature; SSRT. However, the effect of short-range ordering during deformation was considered to have negligible in this study, since the test conditions of all tests and chemical composition of every specimen was maintained to be same [69]–[71], [85], [86].

## 4.3. PWSCC initiation of notched specimen

The trend observed in notched specimen was somewhat different with that of smooth specimen; 20 years thermally aged specimen has the highest susceptibility to PWSCC initiation. To find out the reason for this, surface cracking behavior was observed in notched specimen. As shown in Figure 4-3, cracks were observed not at the center of notch where hydrostatic stress should be the highest, rather observed at the region far from the center. From stress analysis result, shown in Figure 4-4, this region was revealed to have high shear stress component than the central region. In this figure, shear stress was decided as the stress component which have 45° from the tangent line at the surface element of notched surface. Stress triaxiality was defined by von mises stress divided by mean stress. From this observation, it could be thought that the PWSCC initiation behavior under triaxial stress might be controlled by shear stress component.

Further investigation at fracture surface of cracks shows stair shape of fracture surface as shown in Figure 4-5. Those were observed in notched specimen only. It is called pseudo-intergranular cracking, which indicates the cracking behavior which propagate through grain boundary then grain matrix, one by one. As the result, the fracture surface shows stair shape. This is large difference with those of intergranular cracking, which shows flat fracture surface as shown in Figure 4-5.

Pseudo-intergranular cracking was reported in several nickel-based alloys. Those were formed by enhanced localized plasticity, majorly occurred by localized corrosion due to shear stress concentration or hydrogen absorption. Concentration of hydrogen might cause the embrittlement of grain boundary, which in turns cause cracking of matrix, since the grain boundary is too hardened to be broken which is major crack path in nickel-based alloy. This phenomenon cause breaking of grain matrix and leave trace as stair shape of fracture surface [82], [87]–[91]. Also, hydrogen diffusion or adsorption could be enhanced by localized shear stress, since shear stress could activate multiple slip systems which could promote diffusion of hydrogen along grain boundary. Also, enhanced localized plasticity, which occurred by dislocation pile-up at grain boundary due to deformation or promote diffusion of dislocation,

could induce grain boundary embrittlement and cause similar results [90], [91]. This observation clearly shows the effect of shear stress induced by triaxial stress to PWSCC initiation susceptibility of nickel-based alloy. Note that shear stress could be induced at the region near the round notch, since triaxial stress induced at round notch could be dispersed compare to induced at sharp notched region [92]–[94]. Also, hydrogen diffusion or localized plasticity could be enhanced mainly due to shear stress, not triaxial stress, therefore, the specimen geometry should also be carefully investigated to evaluate whether triaxial stress influences PWSCC initiation or not [95]–[97].

To find out proper model parameter for PWSCC initiation behavior of notched specimen, critical resolved shear stress (CRSS) was calculated with the material factor obtained in this study. Relevant equation is shown in below. In this equation, G is shear modulus, b is burgers vector, r is radius of precipitates, f is volume fraction of precipitates, and delta z is range of precipitates in z-direction. Through the calculation with the parameters in Table 3-3, same trend was observed between CRSS and SCC initiation time of notched specimen as shown in Figure 4-6. Since CRSS stands for the resistance of material to shear stress, the share stress might responsible to induce PWSCC at notched specimen. And it was confirmed at surface cracking morphology and stress intensity calculation as shown in Figure 4-4. Most of cracks were observed at the region where shear stress is high.

$$\boldsymbol{\Delta\tau = \frac{Gb}{r}\left(\frac{3}{2\pi}\right)\left(\frac{V\Delta Z}{r}\right)^{0.5}} \qquad (4)$$

## 4.4. PWSCC initiation model

Based on the parameters described in section 4, modification was attempted based on the PWSCC initiation model of Garud [42]. Garud established a PWSCC initiation model based on ASME Code Section III. This model was designed to explain the effect of cold work to effective stress and deformation response. And widely used as important PWSCC initiation model in many papers regarding PWSCC initiation of nickel-based alloys in mechanical point of view. Several missing parts of this model is that, this model consider the effect of material parameter by single parameter which is deduced from the fitting results based on several experimental results. Also, this model does not consider the effect of triaxial stress.

$$t_i = \lambda_e \ln[A] \frac{\ln[\frac{A-z}{\sigma/\sigma_y - z}]}{\ln[\frac{A-z}{1-z}] m^q} \quad (1)$$

$\lambda_e$ = Non-cold work related factor

$A$ = Cold work-SCC microcracking resistance $= vexp[wr]$

$z$ = Cold work-SCC threshold $= z_1 + z_2 \ln(r)$

$r$ = Strength ratio $= \frac{\sigma_u}{\sigma_y}$

σ = Applied stress

$\sigma_y$ = Yield stress

$\sigma_u$ = Ultimate tensile stress

$m$ = Measure of cold work $= k\left(\frac{S_y}{E}\right)^a (r-1)^b (r)^c$

$E$ = Young's modulus

q = Empirical constant defining $a_n$ in terms of m

$a_n$ = Cold work-SCC environmental resistance $= 1/m^q$

$a, b, c, k, z_1, z_2$ = Empirical constants

To make the model consider both long-term thermal aging and triaxial stress, three parameters were inserted to the model above; triaxial stress parameter, parameter for Orowan mechanism and parameter from CRSS.

$$\sigma_{TS} = \frac{\sigma_m}{\sigma_{eq}} \quad (5)$$

$$O = \frac{Gb}{L-2r} \quad (6)$$

$$C = Gb\left(\frac{3}{2\Pi}\right) A_{CRSS},\ A_{CRSS} = \frac{1}{r}\left(\frac{f\Delta z}{r}\right)^{0.5} \quad (7)$$

Triaxial stress often defined as the mean stress divided by equivalent von mises stress, therefore, parameter shown in equation 5 was inserted to model to make the model. Parameters from Orowan mechanism and CRSS are calculated in this study and shown in equation 6 and 7. By inserting above parameters, modified Garud equation is established as below. Fitting parameters were deduced via functional fitting; A was 0.1, B was 0.04.

$$t_i = \frac{A \times C}{O \times B \times \sigma_{TS}} \times C_n \tag{8}$$

$$C_n = \lambda_e \ln[A] \frac{\ln[\frac{A-z}{\sigma/\sigma_y - z}]}{\ln[\frac{A-z}{1-z}] m^q} \tag{9}$$

Meanwhile, to validate the model suggested, comparison with previous data should be considered to do parametric calibration or calibrate the fitting parameters of this study. However, there exist few studies which report the data needed for this model such as fraction of precipitates or length between precipitates [6], [15], [98], [99]. To compensate the lack of data, fitting was conducted based on the results observed in this study. To parameters was fitted; area fraction of precipitates and distance between precipitates, since both PWSCC initiation time of smooth and notched specimen are affected by both parameters. Fitting results are shown in Figure 4-7 and Figure 4-8. Both parameters were plotted based on the changes of radius of precipitates since radius of precipitates are increased during thermal aging, therefore, it could represent the effect of thermal aging. Area fraction of precipitates were increased by thermal aging while distance between precipitates were decreased at early stage of thermal aging and increased in later stage of thermal aging.

Based on the parameters calculated based on the fitting, calculation was conducted according to the PWSCC initiation model proposed in this study as shown in Figure 4-9. Similar trends were observed in the calculation results: under monoaxial stress state, where triaxiality is 0.33 (smooth specimen), PWSCC initiation time is decreased in early stage of thermal aging and increased in latter stage of thermal aging, while PWSCC initiation time is decreased gradually when triaxiality is 0.5 (notched specimen). However, it should be noted that these results are calculated based on limited situation, where shear stress is induced due to specimen shape and notch shape at the surface of specimen.

To validate the model, PWSCC initiation time was calculated and plotted as shown in Figure 4-9 and Figure 4-9. It was hard to find suitable studies which could be used to validation, since the precipitate size or fraction was not investigated and hard to be quantified [100]–[102]. Several studies

provide the grain boundary precipitate fraction of their study. And those were plotted in Figure 4-9.

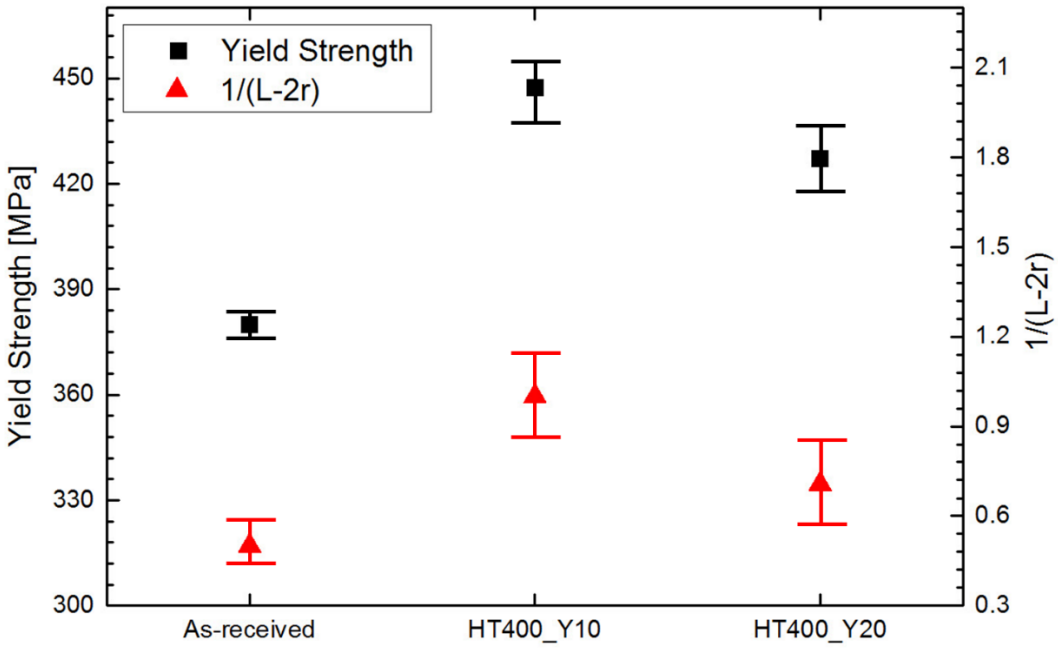


Figure 4-1. Comparison of yield strength with calculation results according to Orowan mechanism. Each are distinguished with different colors and symbols.

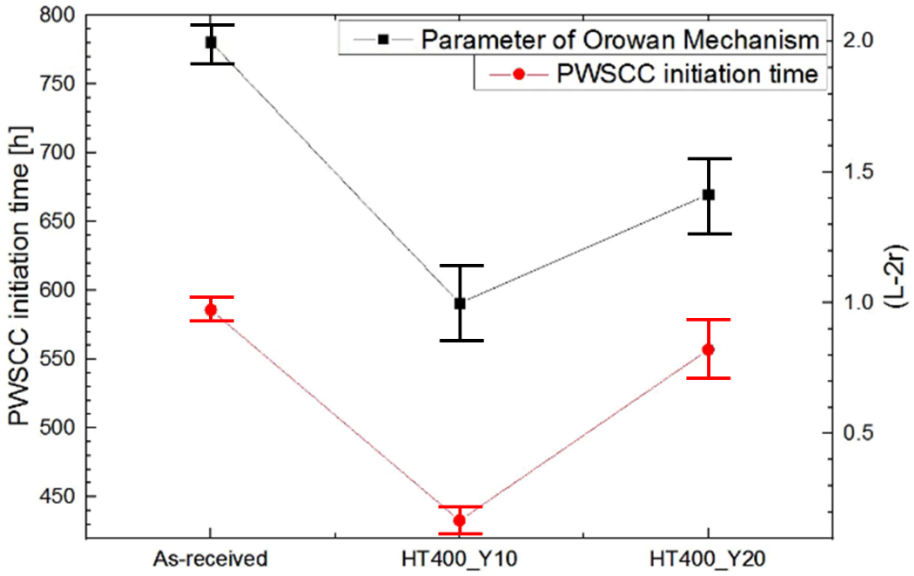


Figure 4-2. Calculation results based on Orowan Mechanism and comparison with the PWSCC initiation time.

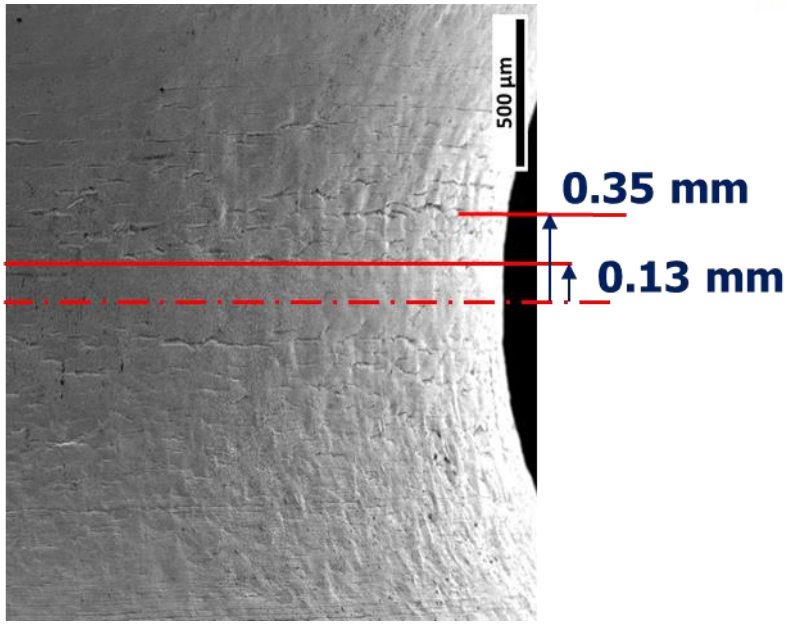


Figure 4-3. Surface cracking morphology of notched specimen. Cracks were observed not at the center of specimen, but at the region away from the center.

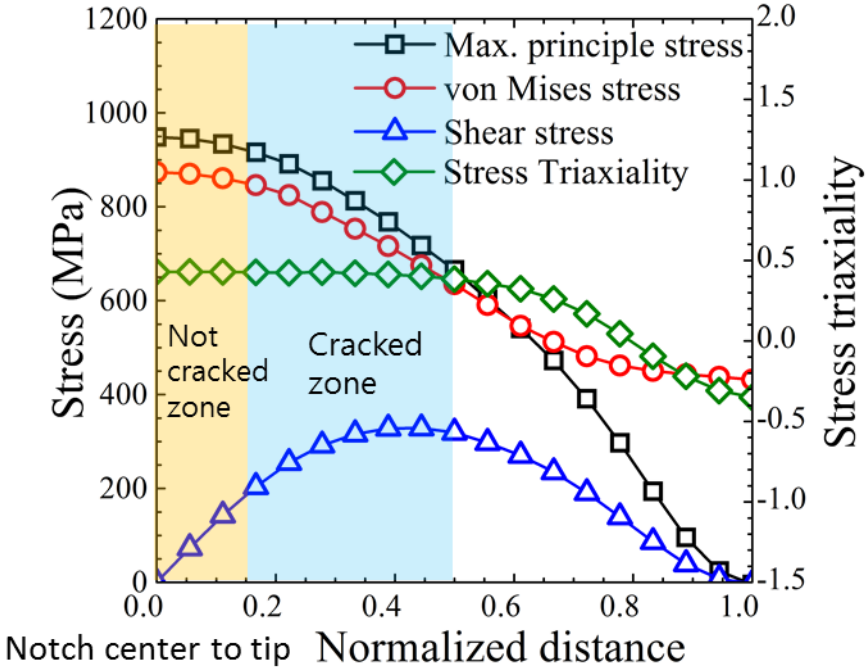


Figure 4-4. Stress analysis results conducted at the surface of notched specimen. Note that cracking was occurred at the region where shear stress is high.

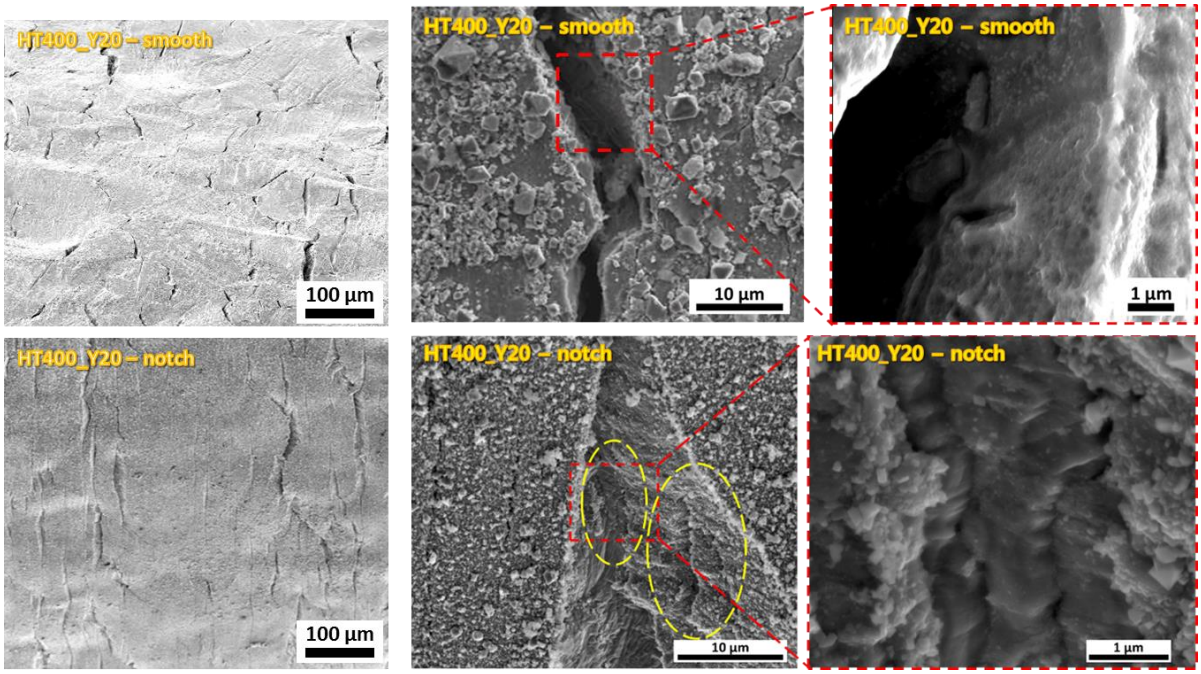


Figure 4-5. SEM images of crack fracture surface of smooth and notched specimens. It is magnified as it goes to right. Stair shape fracture surface was observed at notched specimen, while those were not observed in smooth specimen.

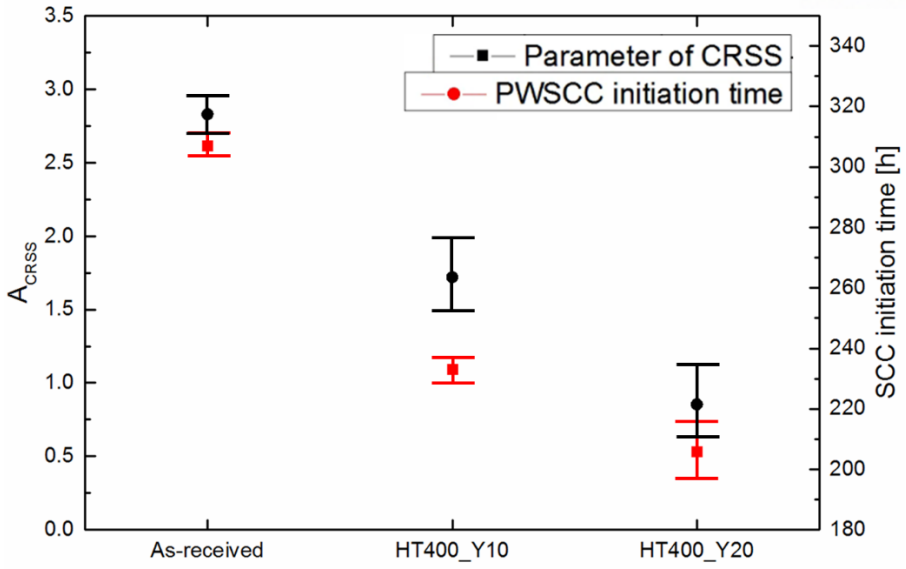


Figure 4-6. Critical resolved shear stress calculation results based on the precipitate parameters achieved in this study. Same trend was observed with PWSCC initiation time of notched specimen.

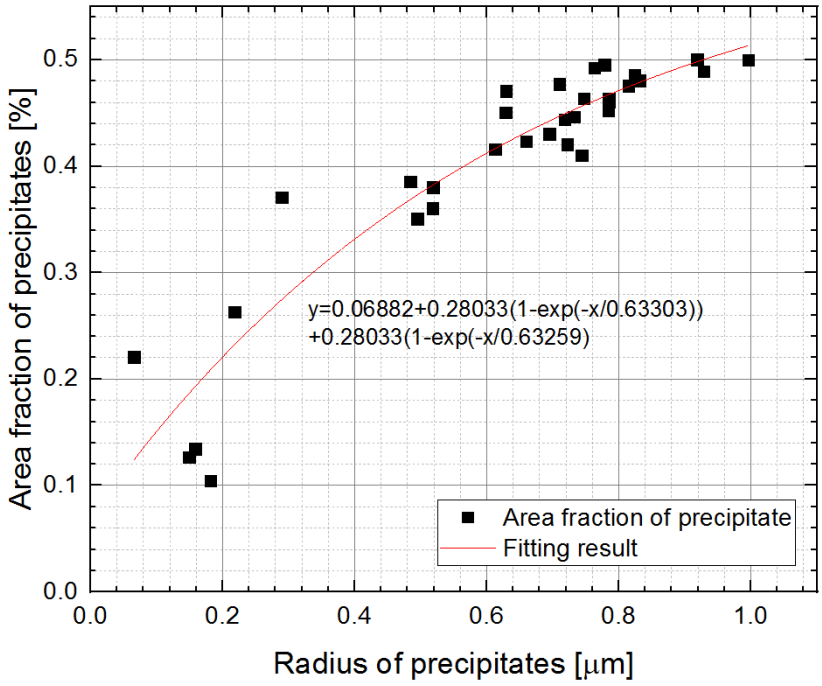


Figure 4-7. Fitting result to estimate area fraction of precipitates based on the results observed in this study

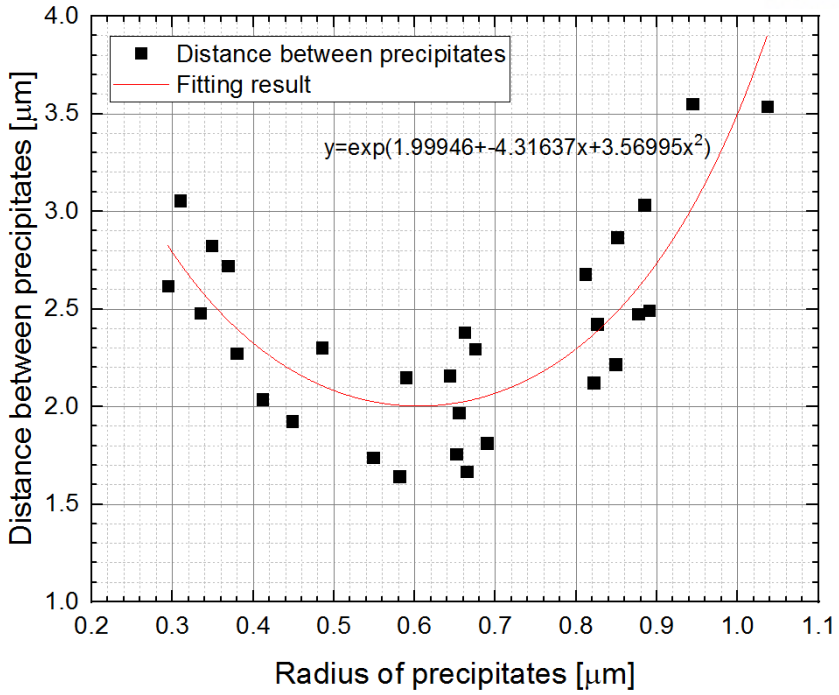


Figure 4-8. Fitting result to estimate distance between precipitates based on the results observed in this study.

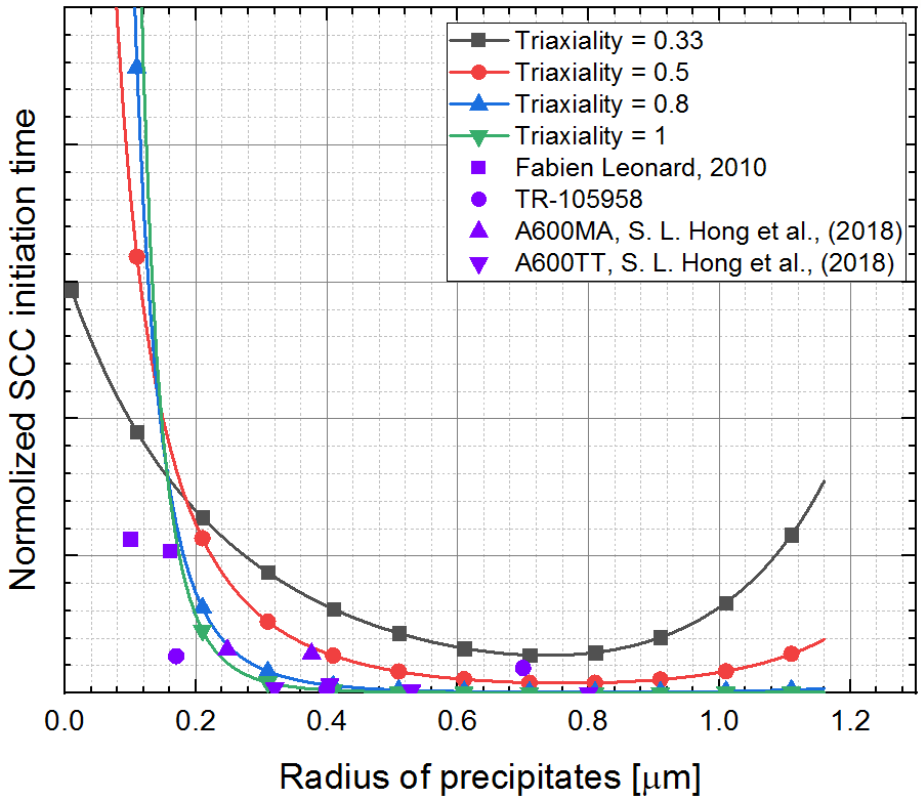


Figure 4-9. Calculation result of proposed model in this study. Normalized PWSCC initiation time was plotted based on the radius of precipitates. Triaxiality of 0.33 indicates smooth specimen, 0.5 indicated notched specimen in this study. PWSCC initiation time was decreased as triaxiality increased [100]–[102].

# 5. Conclusion

In this research, PWSCC initiation behavior of Alloy 600 was investigated by considering two parameters; long-term thermal aging and triaxial stress. The research covers from experimental setup to model validation, and it could be concluded as follows:

1) Effect of long-term thermal aging

The most remarkable change was occurred in precipitate morphology. The length of precipitates was not changed while the number fraction of that was increased during 10 years of thermal aging. Meanwhile, length of precipitates was increased and number fraction of that was not changed during 20 years of thermal aging. This change lead to three big changes which listed next: 1) hardening and softening of mechanical properties, 2) PWSCC initiation behavior under monoaxial stress and 3) PWSCC initiation behavior under triaxial stress.

The tensile properties of 10 years thermally aged specimen were the highest, while elongation of it was the minimum. Also, same trend was observed at PWSCC susceptibility test with smooth specimen; the PWSCC initiation susceptibility of 10 years thermally aged specimen was the highest. From this fact, it could be concluded that PWSCC initiation behavior of nickel-based alloy is closed related to precipitate morphology and could be explained by Orowan Mechanism.

2) Effect of triaxial stress

From the SSRT results of notched specimen, several interesting results were observed; no cracks were existed at the center of notch of notched specimen and stair shape of fracture surface was observed. Both features are the evident that shear stress is an important factor which determine the PWSCC initiation susceptibility of nickel-based alloys. Therefore, critical resolved shear stress which is the parameter that signified the resistance of material to shear stress was calculated. And calculation result has same trend with that of PWSCC initiation of notched specimen.

3) Two parameters and PWSCC initiation model

Two parameters were deduced from the study; parameter from Orowan Mechanism and from critical resolved shear stress. Those were inserted to initiation model of Garud and seems fitted well with several previous experimental results.

However, the use of the model could be limited by following assumptions and realities. There are too many assumptions to use this study, since precipitate morphology cause many changes in material properties such as grain orientation, carbide morphologies, residual stress, phase distribution, and so on. Also, most of current studies are focused on mechanical properties such as yield strength and material properties such as grain boundary misorientation. However, this study emphasizes the importance of morphology of precipitates, specifically distance or distribution of them, which was not considered until now. Whether or not, it is hard to calculate with this model to estimate the PWSCC initiation time now.

Nonetheless, this research emphasize that the morphology of precipitates could influence not only strength of material, but also change PWSCC initiation susceptibility under various stress conditions. Also, triaxial stress and corresponding shear stress could change the susceptibility to PWSCC initiation of Alloy 600. Therefore, it would be desirable to recommend researchers to investigate the precipitate morphology of their material. And with that effort, it is believed that the effect of long-term thermal aging and triaxial stress could be more clarified and considered properly in future.

# REFERENCES


[1] T. M. Pollock and S. Tin, "Nickel-Based Superalloys for Advanced Turbine Engines: Chemistry, Microstructure and Properties," *J. Propuls. Power*, vol. 22, no. 2, pp. 361–374, 2006.

[2] K. Sieradzki and R. C. Newman, "Stress-Corrosion Cracking," *J. Phys. Chem. Solids*, vol. 48, no. 11, pp. 1101–1113, 1987.

[3] C. J. McMahon and L. F. Coffin, "Mechanisms of damage and fracture in high-temperature, low-cycle fatigue of a cast nickel-based superalloy," *Metall. Trans.*, vol. 1, no. 12, pp. 3443–3450, 1970.

[4] R. A. Stevens and P. E. J. Flewitt, "The effects of γ′ precipitate coarsening during isothermal aging and creep of the nickel-base superalloy IN-738," *Mater. Sci. Eng.*, vol. 37, no. 3, pp. 237–247, 1979.

[5] T. H. Lee, I. S. Hwang, H. D. Kim, and J. H. Kim, "Techniques for intergranular crack formation and assessment in alloy 600 base and alloy 182 weld metals," *Nucl. Eng. Technol.*, vol. 47, no. 1, pp. 102–114, 2015.

[6] S. S. Hwang, Y. S. Lim, S. W. Kim, D. J. Kim, and H. P. Kim, "Role of grain boundary carbides in cracking behavior of Ni base alloys," *Nucl. Eng. Technol.*, vol. 45, no. 1, pp. 73–80, 2013.

[7] V. S. Raja and T. Shoji, *Stress corrosion cracking: Theory and practice*. 2011.

[8] P. M. Scott, "An Overview of Internal Oxidation as a Possible Explanation of Intergranular Stress Corrosion Cracking of Alloy 600 in PWRS," in *Ninth International Symposium on Environmental Degradation of Materials in Nuclear Power Systems-Water Reactors*, 2013, pp. 1–14.

[9] S. C. Yoo, K. J. Choi, C. B. Bahn, S. H. Kim, J. Y. Kim, and J. H. Kim, "Effects of thermal aging on the microstructure of Type-II boundaries in dissimilar metal weld joints," *J. Nucl. Mater.*, vol. 459, pp. 2–12, 2015.

[10] M. Casales, V. M. Salinas-Bravo, A. Martinez-Villafañe, and J. G. Gonzalez-Rodriguez, "Effect of heat treatment on the stress corrosion cracking of alloy 690," *Mater. Sci. Eng. A*, vol. 332, no. 1–2, pp. 223–230, 2002.

[11] E. L. Hall and C. L. Briant, "The microstructural response of mill-annealed and solution-annealed INCONEL 600 to heat treatment," *Metall. Trans. A*, vol. 16, no. 7, pp. 1225–1236, 1985.

[12] J. J. Kai, G. P. Yu, C. H. Tsai, M. N. Liu, and S. C. Yao, "The effects of heat treatment on the chromium depletion, precipitate evolution, and corrosion resistance of INCONEL alloy 690,"

*Metall. Trans. A*, vol. 20, no. 10, pp. 2057–2067, 1989.

[13] R. Celin and F. Tehovnik, "DEGRADATION OF A Ni-Cr-Fe ALLOY IN A PRESSURISED-WATER NUCLEAR POWER PLANT," *Mater. Tehnol.*, vol. 45, no. 2, pp. 151–157, 2011.

[14] K. J. Choi, S. H. Shin, J. J. Kim, J. A. Jung, and J. H. Kim, "Three dimensional atom probe study of Ni-base alloy/low alloy steel dissimilar metal weld interfaces," *Nucl. Eng. Technol.*, vol. 44, no. 6, pp. 673–682, 2012.

[15] W. Bamford and J. Hall, "A review of alloy 600 cracking in operating nuclear plants: historical experience and future trends," *11th Int. Conf. Environ. Degrad. Mater. Nucl. Power Syst. — Water React.*, 2003.

[16] H. Miyamoto, D. Saburi, and H. Fujiwara, "A microstructural aspect of intergranular stress corrosion cracking of semi-hard U-bend tubes of commercially pure copper in cooling systems," *Eng. Fail. Anal.*, vol. 26, pp. 108–119, 2012.

[17] Y. S. Lim, H. P. Kim, and S. S. Hwang, "Microstructural characterization on intergranular stress corrosion cracking of Alloy 600 in PWR primary water environment," *J. Nucl. Mater.*, vol. 440, no. 1–3, pp. 46–54, 2013.

[18] S. Nishikawa, Y. Horii, and K. Ikeuchi, "Effect of chromium content on stress corrosion cracking susceptibility of shielded metal arc weld metals for 600 type alloy in high-temperature pressurised pure water," *Weld. Int.*, vol. 27, no. 6, pp. 450–459, 2013.

[19] Q. Peng, J. Hou, Y. Takeda, and T. Shoji, "Effect of chemical composition on grain boundary microchemistry and stress corrosion cracking in Alloy 182," *Corros. Sci.*, vol. 67, pp. 91–99, 2013.

[20] J. H. Kim, Y. J. Oh, I. S. Hwang, D. J. Kim, and J. T. Kim, "Fracture behavior of heat-affected zone in low alloy steels," *J. Nucl. Mater.*, vol. 299, no. 2, pp. 132–139, 2001.

[21] J. H. Kim and R. G. Ballinger, "Stress corrosion cracking crack growth behavior of type 316L stainless steel weld metals in boiling water reactor environments," *Corrosion*, vol. 64, no. 8, pp. 645–656, 2008.

[22] T.-F. Chen, G. P. Tiwari, Y. Iijima, and K. Yamauchi, "Volume and grain boundary diffusion of chromium in Ni-base Ni-Cr-Fe alloys," *Mater. Trans.*, vol. 44, no. 1, pp. 40–46, 2003.

[23] P. M. Scott, "An overview of materials degradation by stress corrosion in PWRs," *Eur. Fed. Corros. Publ.*, vol. 51, p. 3, 2007.

[24] M. J. O. M. B. Toloczko D. K. Schreiber, S. M. Bruemmer, "Corrosion and stress corrosion crack initiation of cold-worked alloy 690 in PWR primary water," *Tech. Milestone Rep.*, 2013.

[25] J. Panter, B. Viguier, J. M. Cloue, M. Foucault, P. Combrade, and E. Andrieu, "Influence of oxide films on primary water stress corrosion cracking initiation of alloy 600," *J. Nucl. Mater.*, vol. 348, no. 1–2, pp. 213–221, 2006.

[26] K. J. Choi, S. H. U. N. Shin, J. I. H. J. I. N. Kim, J. U. a N. G. Jung, and J. I. H. J. I. N. Kim, "Nano-Structural and Nano-Chemical Analysis of Ni-Base Alloy / Low Alloy Steel Dissimilar Metal Weld Interfaces," *Nucl. Eng. Technol.*, vol. 44, no. 5, pp. 491–500, 2012.

[27] G. S. Was, "Grain-Boundary Chemistry and Intergranular Fracture in Austenitic Nickel-Base Alloys—A Review," *Corrosion*, vol. 46, no. 4, pp. 319–330, Apr. 1990.

[28] J. J. H. Kim, K. J. Choi, C. B. Bahn, and J. J. H. Kim, "In situ Raman spectroscopic analysis of surface oxide films on Ni-base alloy/low alloy steel dissimilar metal weld interfaces in high-temperature water," *J. Nucl. Mater.*, vol. 449, no. 1–3, pp. 181–187, 2014.

[29] H. O. Nam, I. S. Hwang, K. H. Lee, and J. H. Kim, "A first-principles study of the diffusion of atomic oxygen in nickel," *Corros. Sci.*, vol. 75, pp. 248–255, 2013.

[30] J. H. Kim and S. Hwang, "Development of an in situ Raman spectroscopic system for surface oxide films on metals and alloys in high temperature water," *Nucl. Eng. Des.*, vol. 235, no. 9, pp. 1029–1040, 2005.

[31] K. J. Choi, J. J. Kim, B. H. Lee, C. B. Bahn, and J. H. Kim, "Effects of thermal aging on microstructures of low alloy steel-Ni base alloy dissimilar metal weld interfaces," *J. Nucl. Mater.*, vol. 441, no. 1–3, pp. 493–502, 2013.

[32] J. H. Kim and I. S. Hwang, "Electroless nickel-plating for the PWSCC mitigation of nickel-base alloys in nuclear power plants," *Nucl. Eng. Des.*, vol. 238, no. 10, pp. 2529–2535, 2008.

[33] S. A. Tukur, M. S. Dambatta, A. Ahmed, N. M. Muaz, N. M. Mu'az, and N. M. Mu'az, "Effect of Heat Treatment Temperature on Mechanical Properties of the AISI 304 Stainless Steel," *Intl J Innov Res Sci, Eng Technol*, vol. 3, pp. 9516–9520, 2014.

[34] S. C. Yoo, K. J. Choi, T. Kim, S. H. Kim, J. Y. Kim, and J. H. Kim, "Microstructural evolution and stress-corrosion-cracking behavior of thermally aged Ni-Cr-Fe alloy," *Corros. Sci.*, vol. 111, pp. 39–51, 2016.

[35] S. C. Yoo, K. J. Choi, T. Kim, and J. H. Kim, "Effects of thermal aging and stress triaxiality on PWSCC initiation susceptibility of nickel-based Alloy 600," *J. Mech. Sci. Technol.*, 2016.

[36] ASTM International.; American Society for Testing and Materials, "Standard Practice for Making and Using C-Ring Stress-Corrosion Test Specimens," *Des. G 38 – 01 (Reapproved 2007)*, 2007.

[37] J.-Y. Jeon, Y.-J. Kim, and J.-W. Kim, "Burst Pressure Prediction of Cracked Steam Generator Tube Using FE Damage Analysis," 2015.

[38] S. Ritter and H. P. Seifert, "Effect of corrosion potential on the corrosion fatigue crack growth behaviour of low-alloy steels in high-temperature water," *J. Nucl. Mater.*, vol. 375, no. 1, pp. 72–79, 2008.

[39] K. Nakacho *et al.*, "Measurement of welding residual stresses of reactor vessel by inherent

strain method: Measurement of residual stresses of pipe-plate penetration joint," *Weld. Int.*, 2009.

[40] J. K. Benz, J. H. Kim, and R. G. Ballinger, "Effect of Oxygen Potential on Crack Growth in Alloys for Advanced Energy Systems," *J. Eng. Gas Turbines Power*, vol. 132, no. 10, p. 102901, 2010.

[41] I. S. Hwang, S. U. Kwon, J. H. Kim, and S.-G. Lee, "An Intraspecimen Method for the Statistical Characterization of Stress Corrosion Crack Initiation Behavior," *Corrosion*, vol. 57, no. 9, pp. 787–793, 2001.

[42] Y. S. Garud, "SCC initiation model and its implementation for probabilistic assessment," in *American Society of Mechanical Engineers, Pressure Vessels and Piping Division (Publication) PVP*, 2010, vol. 6, pp. 615–620.

[43] W. T. Tsai, C. L. Yu, and J. I. Lee, "Effect of heat treatment on the sensitization of Alloy 182 weld," *Scr. Mater.*, vol. 53, no. 5, pp. 505–509, Sep. 2005.

[44] T. Shoji, Z. Lu, and H. Murakami, "Formulating stress corrosion cracking growth rates by combination of crack tip mechanics and crack tip oxidation kinetics," *Corros. Sci.*, vol. 52, no. 3, pp. 769–779, 2010.

[45] J. M. Boursier, F. Vaillant, and B. Yrieix, "Weldability, thermal aging and PWSCC behavior of nickel weld metals containing 15 to 30% chromium," in *ASME/JSME 2004 Pressure Vessels and Piping Conference*, 2004, pp. 109–121.

[46] W. C. Oliver and G. M. Pharr, "Measurement of hardness and elastic modulus by instrumented indentation: Advances in understanding and refinements to methodology," *J. Mater. Res.*, vol. 19, no. 1, pp. 3–20, 2004.

[47] E. Richey, D. S. Morton, and M. K. Schurman, "SCC initiation testing of nickel-based alloys using in-situ monitored uniaxial tensile specimens," in *12th International Conference on Environmental Degradation of Materials in Nuclear Power System*, 2005.

[48] E. Richey, D. S. Morton, R. A. Etien, G. A. Young, and R. B. Bucinell, *SCC initiation in Alloy 600 heat affected zones exposed to high temperature water*. New Orleans, LO: United States. Department of Energy, 2008.

[49] S. A. Sajjadi and S. M. Zebarjad, "Effect of temperature on tensile fracture mechanisms of a Ni-base superalloy," *Arch. Mater. Sci. Eng.*, vol. 28, no. 1, pp. 34–40, 2007.

[50] A. Shyam and W. W. Milligan, "Effects of deformation behavior on fatigue fracture surface morphology in a nickel-base superalloy," *Acta Mater.*, vol. 52, no. 6, pp. 1503–1513, 2004.

[51] Y. Zhao, I. C. Choi, Y. J. Kim, and J. Il Jang, "On the nanomechanical characteristics of thermally-treated alloy 690: Grain boundaries versus grain interior," *J. Alloys Compd.*, vol. 582, pp. 141–145, 2014.

[52] J. Chen and S. J. Bull, "On the relationship between plastic zone radius and maximum depth during nanoindentation," *Surf. Coatings Technol.*, vol. 201, no. 7 SPEC. ISS., pp. 4289–4293, 2006.

[53] Q. Peng, J. Hou, K. Sakaguchi, Y. Takeda, and T. Shoji, "Effect of dissolved hydrogen on corrosion of Inconel Alloy 600 in high temperature hydrogenated water," *Electrochim. Acta*, vol. 56, no. 24, pp. 8375–8386, 2011.

[54] K. Mo, G. Lovicu, X. Chen, H. M. Tung, J. B. Hansen, and J. F. Stubbins, "Mechanism of plastic deformation of a Ni-based superalloy for VHTR applications," *J. Nucl. Mater.*, vol. 441, no. 1–3, pp. 695–703, 2013.

[55] J. M. Pardal, S. S. M. Tavares, V. F. Terra, M. R. Da Silva, and D. R. Dos Santos, "Modeling of precipitation hardening during the aging and overaging of 18Ni–Co–Mo–Ti maraging 300 steel," *J. Alloys Compd.*, vol. 393, no. 1, pp. 109–113, 2005.

[56] H. Grimmer, W. Bollmann, and D. H. Warrington, "Coincidence-ste lattices and complete patter-shift lattices in cubic crystals," *Acta Crystallogr A*, vol. 30, no. 2, pp. 197–207, 1974.

[57] L. Tan, K. Sridharan, and T. R. Allen, "Effect of thermomechanical processing on grain boundary character distribution of a Ni-based superalloy," *J. Nucl. Mater.*, vol. 371, no. 1–3, pp. 171–175, 2007.

[58] B. Sunil Kumar, B. S. Prasad, V. Kain, and J. Reddy, "Methods for making alloy 600 resistant to sensitization and intergranular corrosion," *Corros. Sci.*, vol. 70, pp. 55–61, 2013.

[59] D. G. Brandon, B. Ralph, S. Ranganathan, and M. S. Wald, "A field ion microscope study of atomic configuration at grain boundaries," *Acta Metall.*, vol. 12, no. 7, pp. 813–821, 1964.

[60] S. Xia, H. Li, T. G. Liu, and B. X. Zhou, "Appling grain boundary engineering to Alloy 690 tube for enhancing intergranular corrosion resistance," *J. Nucl. Mater.*, vol. 416, no. 3, pp. 303–310, 2011.

[61] H. U. Hong, B. S. Rho, and S. W. Nam, "Correlation of the M23C6 precipitation morphology with grain boundary characteristics in austenitic stainless steel," *Mater. Sci. Eng. a-Structural Mater. Prop. Microstruct. Process.*, vol. 318, no. 1–2, pp. 285–292, 2001.

[62] J. Hou, Q. Peng, Y. Takeda, J. Kuniya, and T. Shoji, "Microstructure and stress corrosion cracking of the fusion boundary region in an alloy 182-A533B low alloy steel dissimilar weld joint," *Corros. Sci.*, vol. 52, no. 12, pp. 3949–3954, 2010.

[63] W. Kuang and G. S. Was, "The effects of grain boundary carbide density and strain rate on the stress corrosion cracking behavior of cold rolled Alloy 690," *Corros. Sci.*, vol. 97, pp. 107–114, 2015.

[64] G. S. Was, H. H. Tischner, and R. M. Latanision, "The Influence of Thermal-Treatment on the Chemistry and Structure of Grain-Boundaries in Inconel 600," *Metall. Trans. a-Physical*

*Metall. Mater. Sci.*, vol. 12, no. 8, pp. 1397–1408, 1981.

[65] J. Huang, X. Wu, and E. H. Han, "Influence of pH on electrochemical properties of passive films formed on Alloy 690 in high temperature aqueous environments," *Corros. Sci.*, vol. 51, no. 12, pp. 2976–2982, 2009.

[66] D. H. Hur and Y. S. Park, "Effect of temperature on the pitting behavior and passive film characteristics of alloy 600 in chloride solution," *Corrosion*, vol. 62, no. 9, pp. 745–750, 2006.

[67] A. P. Majidi and M. A. Streicher, "The Double Loop Reactivation Method for Detecting Sensitization in AISI 304 Stainless Steels," *CORROSION*, vol. 40, no. 11, pp. 584–593, Nov. 1984.

[68] P. NOVAK, R. STEFEC, and F. FRANZ, "Testing the Susceptibility of Stainless Steel to Intergranular Corrosion by a Reactivation Method," *CORROSION*, vol. 31, no. 10, pp. 344–347, Oct. 1975.

[69] S. Kim, D. W. Kim, and Y. S. Kim, "Primary water stress corrosion cracking (PWSCC) mechanism based on ordering reaction in Alloy 600," *Met. Mater. Int.*, vol. 19, no. 5, pp. 969–974, 2013.

[70] L. Zhang and J. Wang, "Effect of dissolved oxygen content on stress corrosion cracking of a cold worked 316L stainless steel in simulated pressurized water reactor primary water environment," *J. Nucl. Mater.*, vol. 446, no. 1–3, pp. 15–26, 2014.

[71] Y. S. Kim, W. Y. Maeng, and S. S. Kim, "Effect of short-range ordering on stress corrosion cracking susceptibility of Alloy 600 studied by electron and neutron diffraction," *Acta Mater.*, vol. 83, no. 0, pp. 507–515, 2015.

[72] B. Alexandreanu, B. Capell, and G. S. Was, "Combined effect of special grain boundaries and grain boundary carbides on IGSCC of Ni-16Cr-9Fe-xC alloys," *Mater. Sci. Eng. A*, vol. 300, no. 1–2, pp. 94–104, 2001.

[73] P. L. A. G.S. Was, "Stress Corrosion Cracking Behavior of Alloys in Aggressive Nuclear Reactor Core Environments ," *Corrosion*, vol. 63, no. 1, pp. 19–45, 2007.

[74] P. L. Andresen and M. M. Morra, "Stress corrosion cracking of stainless steels and nickel alloys in high-temperature water," *Corrosion*, vol. 64, no. 1, pp. 15–29, Jan. 2008.

[75] D. H. Kirkwood, "Precipitate number density in a Ni Al alloy at early stages of ageing," *Acta Metall.*, vol. 18, no. 6, pp. 563–570, 1970.

[76] Z. Guo and W. Sha, "Quantification of Precipitation Hardening and Evolution of Precipitates," *Mater. Trans.*, vol. 43, no. 6, pp. 1273–1282, 2002.

[77] V. Mohles, D. Rönnpagel, and E. Nembach, "Simulation of dislocation glide in precipitation hardened materials," *Comput. Mater. Sci.*, vol. 16, no. 1, pp. 144–150, 1999.

[78] R. W. Hayes and W. C. Hayes, "On the mechanism of delayed discontinuous plastic flow in an

age-hardened nickel alloy," *Acta Metall.*, vol. 30, no. 7, pp. 1295–1301, 1982.

[79] J. R. Crum, K. A. Heck, and T. M. Angeliu, "Effect of different thermal treatments on the corrosion resistance of alloy 690 tubing," Electric Power Research Inst., Palo Alto, CA (USA); Inco Alloys International, Inc., Huntington, WV (USA), 1990.

[80] S. M. Bruemmer and G. S. Was, "Microstructural and microchemical mechanisms controlling intergranular stress corrosion cracking in light-water-reactor systems," *J. Nucl. Mater.*, vol. 216, no. C, pp. 348–363, 1994.

[81] H. Dugdale, D. E. J. Armstrong, E. Tarleton, S. G. Roberts, and S. Lozano-Perez, "How oxidized grain boundaries fail," *Acta Mater.*, vol. 61, no. 13, pp. 4707–4713, 2013.

[82] Z. Lu, T. Shoji, S. Yamazaki, and K. Ogawa, "Characterization of microstructure, local deformation and microchemistry in Alloy 600 heat-affected zone and stress corrosion cracking in high temperature water," *Corros. Sci.*, vol. 58, pp. 211–228, 2012.

[83] J. Kim, S. H. Kim, K. J. Choi, C. B. Bahn, I. S. Hwang, and J. H. Kim, "In-situ investigation of thermal aging effect on oxide formation in Ni-base alloy/low alloy steel dissimilar metal weld interfaces," *Corros. Sci.*, vol. 86, pp. 295–303, 2014.

[84] G. J.abraham, V. Kain, G. K. Dey, and V. S. Raja, "Stability of oxide film formed at different temperatures on Alloy 600 in lithiated environment," *J. Nucl. Mater.*, vol. 437, no. 1–3, pp. 188–195, 2013.

[85] A. Marucco, "Atomic ordering in the NiCrFe system," *Mater. Sci. Eng. A*, vol. 189, no. 1–2, pp. 267–276, 1994.

[86] A. Marucco, "Atomic ordering and α′-Cr phase precipitation in long-term aged Ni3Cr and Ni2Cr alloys," *J. Mater. Sci.*, vol. 30, no. 16, pp. 4188–4194, 1995.

[87] M. Koyama, E. Akiyama, K. Tsuzaki, and D. Raabe, "Hydrogen-assisted failure in a twinning-induced plasticity steel studied under in situ hydrogen charging by electron channeling contrast imaging," *Acta Mater.*, vol. 61, no. 12, pp. 4607–4618, 2013.

[88] Y. Watanabe, V. Kain, and M. Kobayashi, "Electrochemical transients observed during slow strain rate test of alloy 600 in borated and lithiated high temperature water," *Jsme Int. J. Ser. a-Solid Mech. Mater. Eng.*, vol. 45, no. 4, pp. 476–480, 2002.

[89] M. Kuruvilla, T. S. Srivatsan, M. Petraroli, and L. Park, "An investigation of microstructure, hardness, tensile behaviour of a titanium alloy: Role of orientation," *S¯adhan¯a*, vol. 33, no. 3, pp. 235–250, 2008.

[90] S. Benbelaid, M. A. Belouchrani, Y. Assoul, and B. Bezzazi, "Modeling Damage of the Hydrogen Enhanced Localized Plasticity in Stress Corrosion Cracking," *Int. J. Damage Mech.*, vol. 20, no. 6, pp. 831–844, Aug. 2011.

[91] I. H. Katzarov, D. L. Pashov, and A. T. Paxton, "Hydrogen embrittlement I. Analysis of

hydrogen-enhanced localized plasticity: Effect of hydrogen on the velocity of screw dislocations in α -Fe," *Phys. Rev. Mater.*, vol. 1, no. 3, p. 033602, Aug. 2017.

[92] A. M. Agogino, "Notch Effects, Stress State, and Ductility," *J. Eng. Mater. Technol.*, 2010.

[93] A. de A. Neves *et al.*, "Influence of notch geometry and interface on stress concentration and distribution in micro-tensile bond strength specimens," *J. Dent.*, 2008.

[94] N. Bonora, D. Gentile, A. Pirondi, and G. Newaz, "Ductile damage evolution under triaxial state of stress: Theory and experiments," *Int. J. Plast.*, 2005.

[95] A. Khalajhedayati and T. J. Rupert, "Emergence of localized plasticity and failure through shear banding during microcompression of a nanocrystalline alloy," *Acta Mater.*, vol. 65, pp. 326–337, Feb. 2014.

[96] H. Hänninen, M. Ivanchenko, Y. Yagodzinskyy, V. Nevdacha, U. Ehrnstén, and P. Aaltonen, "Dynamic strain aging of Ni-base alloys Inconel 600 and 690," *Proc. Twelfth Int. Conf. Environ. Degrad. Mater. Nucl. Power Syst. React.*, no. January 2016, pp. 1423–1430, 2005.

[97] J. . Ferguson and H. F. Lopez, "Oxidation Products in Inconel Alloys 600 and 690 Under Hydrogenated Steam Environments and Their Role in Stress Corrosion Cracking," *Metall. Mater. Trans. A*, vol. 37A, no. August, pp. 2471–2479, Aug. 2006.

[98] B. Alexandreanu, B. Capell, and G. S. Was, "Combined effect of special grain boundaries and grain boundary carbides on IGSCC of Ni-16Cr-9Fe-xC alloys," *Mater. Sci. Eng. A*, vol. 300, no. 1–2, pp. 94–104, 2001.

[99] S. Y. Persaud, J. Smith, A. Korinek, G. A. Botton, and R. C. Newman, "High resolution analysis of oxidation in Ni-Fe-Cr alloys after exposure to 315℃ deaerated water with added hydrogen," *Corros. Sci.*, vol. 106, pp. 236–248, 2016.

[100] R. C. Newman, T. S. Gendron, and P. M. Scott, "Internal Oxidation and Embrittlement of Alloy 600," in *Ninth International Symposium on Environmental Degradation of Materials in Nuclear Power Systems-Water Reactors*, 2013.

[101] F. Leonard, "Study of Stress Corrosion Cracking of Alloy 600 in High Temperature High Pressure Water - Doctoral thesis," 2010.

[102] S. Le Hong, "Influence of Surface Condition on Primary Water Stress Corrosion Cracking Initiation of Alloy 600," *CORROSION*, vol. 57, no. 4, pp. 323–333, Apr. 2001.

# Acknowledgement

인생에 한 번 뿐일 박사 학위 과정의 마지막을 앞두고 있는 지금, 돌이켜보면 너무나 많은 잊지 못할 인연들이 있었고, 너무나 많은 분들께 도움을 받았다는 것을 다시 한번 깨닫게 됩니다. 모든 분들께 감사를 전하진 못하겠지만, 적어도 이 마지막 페이지를 빌어 감사의 인사를 드리고자 합니다.

학위 과정 내내 지도해주신 김지현 교수님. 아무것도 모르던 저를 항상 이끌어 주시고 격려하여 주셔서 감사합니다. 2012년 학부 과정 시절에 연구실에 들어와 2019년 지금에 이르기까지, 길었던 시간만큼 많은 가르침을 받은 것 같습니다. 연구자로서 한 걸음을 떼고 이전과 같지만 다른 인생을 맞이하려고 하니, 교수님의 지난 가르침이 더욱 와 닿는 것 같습니다. 학위 과정은 마무리되었지만, 아직 가야할 길이 먼 부족한 제자를 잘 부탁드리며, 항상 교수님의 은혜에 보답할 수 있도록 노력하겠습니다.

학위 과정 도중에도 많은 가르침을 주시고, 마지막까지 심사위원으로서 귀중한 의견을 주신 황일순 교수님, 권순용 교수님, 오영진 박사님, 최민재 박사님. 교수님, 박사님들과 함께 제 연구에 대해 논의하고, 제안해주신 의견을 검토하여 반영했던 시간들은 모두 너무나 뜻 깊고 의미 있는 시간이었고, 그 시간들 덕분에 제 연구가 한 단계 더 완성될 수 있었던 것 같습니다. 다시 한번 감사의 말씀드리며, 그 때 해 주신 말씀들은 항상 가슴 속 깊이 간직하도록 하겠습니다.

타지인 울산에 와서 가장 긴 시간 동안 함께했던 연구실 식구들. 너무나 고맙고 고마웠고, 짜증나고 미웠고, 가슴 아프고 슬펐던 기억들 모두 이제는 추억이 되어버릴 것 같습니다. 연구실 식구들의 도움이 없었다면 어땠을 지는 생각하기도 싫을 정도입니다. 연구실에 처음 들어와 아무것도 모르는 저를 도와주신 상훈형, 종진형, 주앙형, 경준형, 상일형, 승현형, 태호형, 광범, 정현. 부족한 저를 잘 따라주고 도와준 정원형, 준혁, 태용, 인영형, 윤주, 정환이까지 모두 감사드립니다. 특히, 경준형, 제 학위 논문의 2저자라고 할 수 있을 만큼 많은 도움을 주셔서, 승현형, 제가 잘 몰랐던 전기화학 분야에 쩔쩔매고 있을 때 격려해주시고 도움을 주셔서, 준혁, 윤주, 학부 과정 중에 바빴을텐데도 혼자 하기 어려운 실험에 관심을 가져 주시고 흔쾌히 도와주셔서, 윤주, 인영형, 급한 실험 일정

에 치여 놓친 중요한 업무를 대신 챙겨 주셔서, 태용, 정환이를 포함한 모든 후배들, 선배랍시고 제대로 챙겨준 것도 없는데 항상 배려해주시고 도와주셔서 감사했습니다. 이렇게 헌신적이고 사려 깊은 사람들과 함께하게 된 것을 항상 행운으로 생각하며, 앞으로 도움에 보답할 수 있도록 노력하겠습니다.

또, 항상 조언을 아끼지 않으시고 물심양면 도와주신 국내외 박사님, 교수님들, 그리고 학생분들께도 감사의 말씀을 드리고 싶습니다. 부산대 반치범 교수님, 세종대 김종성 교수님, 고려대 김윤재 교수님, 카이스트 장창희 교수님, 한국원자력연구원 부식연구팀의 모든 박사님들, 한국수력원자력 중앙연구원 재료기기그룹의 모든 박사님들, 또 김영진 박사님을 포함한 다른 많은 박사님들… 그저 나열하는 것도 힘들만큼 너무나 많은 분들께 도움을 받은 것 같습니다. 이 자리를 빌어 제 연구에 관심을 가져 주시고 조언을 아끼지 않으셨던 모든 분들께 감사의 인사를 드립니다.

대학원 생활 내내 저의 힘의 되어주고 힘들 때 서로 의지할 수 있었던 친구들에게도 감사의 인사를 전합니다. 대학교 1학년 때부터 언제나 응원해주었고 고민을 털어놓을 수 있었던 정식형, 연구실 멤버들 못지않게 저를 도와준 지현이를 포함한 유체패밀리, kt낙하산팀, 10멤버들 모두 감사합니다.

마지막으로, 연락도 자주 안하고 늘 바빴던 아들을 격려해주시고 응원해주신 부모님, 가을, 가원, 모두 감사드립니다. 부모님께서 항상 든든하게 기다려 주시고 뒤를 받쳐 주셔서 연구에 매진할 수 있었고, 진심 어린 응원 덕분에 힘들고 어려운 일도 모두 이겨낼 수 있었습니다. 저에게 주신 기대와 은혜만큼 보답하는 아들이 되겠습니다. 또, 항상 어린 손자를 걱정해주신 할머니를 포함한 모든 친척분들께도 감사의 말씀을 드립니다.

아직도 머릿속을 맴도는 너무나 많은 고마우신 분들이 계시지만, 앞으로 만날 날이 더 많을 것이기에, 부족한 감사의 인사는 다른 기회를 빌어야 할 것 같습니다. 다시 한번 모든 분들께 진심으로 감사드립니다.

유승창 올림